

**Title: Modelling the response to vaccine in Non-Human Primates to define
SARS-CoV-2 mechanistic correlates of protection**

Authors: Marie Alexandre¹, Romain Marlin^{2,†}, Mélanie Prague^{1,†}, Séverin Coleon^{3,4}, Nidhal Kahlaoui², Sylvain Cardinaud^{3,4}, Thibaut Naninck², Benoit Delache², Mathieu Surenaud^{3,4}, Mathilde Galhaut², Nathalie Dereuddre-Bosquet², Mariangela Cavarelli², Pauline Maisonnasse², Mireille Centlivre^{3,4}, Christine Lacabartz^{3,4}, Aurelie Wiedemann^{3,4}, Sandra Zurawski⁵, Gerard Zurawski⁵, Olivier Schwartz^{3,6,7}, Rogier W Sanders⁸, Roger Le Grand², Yves Levy^{3,4,9}, Rodolphe Thiébaud^{1,3,10,*}

Affiliations:

¹ Univ. Bordeaux, Department of Public Health, Inserm Bordeaux Population Health Research Centre, Inria SISTM, UMR 1219; Bordeaux, France.

² Center for Immunology of Viral, Auto-immune, Hematological and Bacterial diseases (IMVA-HB/IDMIT), Université Paris-Saclay, Inserm, CEA; Fontenay-aux-Roses, France.

³ Vaccine Research Institute; Creteil, France.

⁴ Inserm U955, Equipe 16; Créteil, France.

⁵ Baylor Scott and White Research Institute and INSERM U955; Dallas, Texas, United States of America.

⁶ Virus & Immunity Unit, Department of Virology, Institut Pasteur; Paris, France.

21 ⁷ CNRS UMR 3569; Paris, France.

22 ⁸ Department of Medical Microbiology, Amsterdam UMC, University of Amsterdam,
23 Amsterdam Infection & Immunity Institute; 1105 AZ Amsterdam, the Netherlands.

24 ⁹ AP-HP, Hôpital Henri-Mondor Albert-Chenevier, Service d'Immunologie Clinique et Maladies
25 Infectieuses; Créteil, France.

26 ¹⁰ CHU Bordeaux, Department of Medical information; Bordeaux, France.

27

28 *Corresponding author: Prof Rodolphe Thiébaud

29 Bordeaux University, Departement of Public Health

30 146 Rue Leo Saignat, 33076 Bordeaux Cedex, France

31 rodolphe.thiebaut@u-bordeaux.fr

32 [†] These authors contributed equally to this work.

33

34 **Key words:** SARS-CoV-2, Correlate of protection, Neutralization, Vaccines

One Sentence Summary: A model-based approach for modelling the immune control of viral dynamics is applied to quantify the effect of several SARS-CoV-2 vaccine platforms and to define mechanistic correlates of protection.

Abstract: The definition of correlates of protection is critical for the development of next generation SARS-CoV-2 vaccine platforms. Here, we propose a model-based approach for identifying mechanistic correlates of protection based on mathematical modelling of viral dynamics and data mining of immunological markers. The application to three different studies in non-human primates evaluating SARS-CoV-2 vaccines based on CD40-targeting, two-component spike nanoparticle and mRNA 1273 identifies and quantifies two main mechanisms that are a decrease of rate of cell infection and an increase in clearance of infected cells. Inhibition of RBD binding to ACE2 appears to be a robust mechanistic correlate of protection across the three vaccine platforms although not capturing the whole biological vaccine effect. The model shows that RBD/ACE2 binding inhibition represents a strong mechanism of protection which required significant reduction in blocking potency to effectively compromise the control of viral replication.

Main Text:

INTRODUCTION

There is an unprecedented effort for SARS-CoV-2 vaccine development with 294 candidates currently evaluated (1). However, variants of concern have emerged before the vaccine coverage was large enough to control the pandemics (2). Despite a high rate of vaccine protection, these variants might compromise the efficacy of current vaccines (3–6). Control of the epidemic by mass vaccination may also be compromised by unknown factors such as long-term protection and the need of booster injections in fragile, immuno-compromised, elderly populations, or even for any individual if protective antibody levels wane. Furthermore, the repeated use of some of the currently approved vaccine could be compromised by potential adverse events or by immunity against vaccine viral vectors (7). Finally, the necessity to produce the billions of doses required to vaccinate the world's population also explains the need to develop additional vaccine candidates.

The identification of correlates of protection (CoP) is essential to accelerate the development of new vaccines and vaccination strategies (8, 9). Binding antibodies to SARS-CoV-2 and *in vitro* neutralization of virus infection are clearly associated with protection (10–13). However, the respective contribution to virus control *in vivo* remains unclear (14), and many other immunological mechanisms may also be involved, including other antibody-mediated functions (antibody-dependent cellular cytotoxicity, antibody-dependent complement deposition, antibody-dependent cellular phagocytosis (11, 15, 16)), as well as T cell immunity (17). Furthermore, correlates of protection may vary between the vaccine platforms (18–21).

Non-human primate (NHP) studies offer a unique opportunity to evaluate early markers of protective response (22, 23). Challenge studies in NHP allow the evaluation of vaccine impact on

the viral dynamics in different tissue compartments (upper and lower respiratory tract) from day one of virus exposure (11, 15, 24). Such approaches in animal models may thus help to infer, for example, the relation between early viral events and disease or the capacity to control secondary transmissions.

Here, we propose to apply a model-based approach on NHP studies to evaluate i) the immune mechanisms involved in the vaccine response, and ii) the markers capturing this/these effect(s) leading to identification of mechanisms of protection and definition of mechanistic CoP (25). First, we present a mechanistic approach based on ordinary differential equation (ODE) models reflecting the virus-host interaction inspired from models proposed for SARS-CoV-2 infection (26–31) and other viruses (32–35). The proposed model includes several new aspects refining the modeling of viral dynamics *in vivo*, in addition to the integration of vaccine effect. A specific inoculum compartment allows distinguishing the virus coming from the challenge inoculum and the virus produced *de novo*, which is a key point in the context of efficacy provided by antigen specific pre-existing immune effectors induced by the vaccine. Then, an original data mining approach is implemented to identify the immunological biomarkers associated with specific mechanisms of vaccine-induced protection.

We apply our approach to a recently published study (36) testing a protein-based vaccine targeting the receptor-binding domain (RBD) of the SARS-CoV-2 spike protein to CD40 (α CD40.RBD vaccine). Targeting vaccine antigens to dendritic cells via the surface receptor CD40 represents an appealing strategy to improve subunit-vaccine efficacy (37–40) and for boosting natural immunity in SARS-CoV-2 convalescent NHP.

We show that immunity induced by natural SARS-CoV-2 infection, as well as vaccine-elicited immune responses contribute to viral load control by i) blocking new infection of target cells and ii) by increasing the loss of infected cells. The modelling showed that antibodies inhibiting

binding of RBD domain to ACE2 correlated with blockade of new infections and RBD binding antibodies correlate with the loss of infected cells, reflecting importance of additional antibody functionalities. The role of RBD/ACE2 binding inhibition has been confirmed in two other vaccine platforms.

RESULTS

A new mechanistic model fits the *in vivo* viral load dynamics in nasopharyngeal and tracheal compartments

The mechanistic model aims at capturing the viral dynamics following challenge with SARS-CoV-2 virus in NHP. For that purpose, we used data obtained from 18 cynomolgus macaques involved in the vaccine study reported by Marlin et al (36) and exposed to a high dose (1×10^6 pfu) of SARS-CoV-2 administered via the combined intra-nasal and intra-tracheal route. The viral dynamics during the primary infections were characterized by a peak of genomic RNA (gRNA) production three days post-infection in both tracheal and nasopharyngeal compartments, followed by a decrease toward undetectable levels beyond day 15 (**Figure 1 – figure supplement 1**). At the convalescent phase (median 24 weeks after the primary infection), 12 macaques were challenged with SARS-CoV-2 a second time, four weeks after being randomly selected to receive either a placebo (n=6) or a single injection of the α CD40.RBD vaccine (n=6) (**Figure 1A**). A third group of 6 naïve animals were infected at the same time. Compared to this naïve group, viral dynamics were blunted following the second challenge of convalescent animals with the lowest viral load observed in vaccinated animals (**Figure 1B, Figure 1 - figure supplement 2**).

We developed a mathematical model to better characterize the impact of the immune response on the viral gRNA and subgenomic RNA (sgRNA) dynamics, adapted from previously published work (26, 27, 41), which includes uninfected target cells (T) that can be infected (I_1) and produce virus after an eclipse phase (I_2). The virus generated can be infectious (V_i) or non-infectious (V_{ni}). Although a single compartment for *de novo* produced viruses (V) could be mathematically considered, two distinct ODE compartments were assumed for a better understanding of the model. We completed the model by a compartment for the inoculum to distinguish between the injected virus (V_s) and the virus produced *de novo* by the host (V_i and V_{ni}). In both compartments of the upper respiratory tract (URT), the trachea and nasopharynx, viral dynamics were distinctively described by this model (**Figure 2A**). Viral exchange between the two compartments was tested (either from the nasopharynx to the trachea or vice versa). However, as described in the literature (28, 42, 43) and demonstrated by the additional modeling work in Appendix 1 “Model building”, viral transport within the respiratory tract plays a negligible role in viral kinetics compared with viral clearance. Consequently, no exchange was considered in the model. Using the gRNA and sgRNA viral loads, we jointly estimated (i.e., shared random effects and covariates) the viral infectivity (β), the viral production rate (P) and the loss rate of infected cells (δ) in the two compartments. We assumed that gRNA and sgRNA were proportional to the free virus and the infected cells, respectively. This modeling choice relied on both biological and mathematical reasons (see section Methods for more details). Due to identifiability issues, the duration of the eclipse phase ($1/k$), the clearance of free viruses from the inoculum (c_i) and produced *de novo* (c) were estimated separately by profile likelihood and assumed to be identical in the two compartments of the URT. In addition, infectious and non-infectious viruses were assumed to be cleared at the same rate. We estimated the viral infectivity at 0.95×10^{-6} ($CI_{95\%}$ [0.18×10^{-6} ; 4.94×10^{-6}]) (copies/ml) $^{-1}$ day $^{-1}$ in naïve animals, which is in the range of previously

reported modelling results whether in the case of SARS-CoV-2 virus (27, 29), or influenza (32, 33). We found estimates of the loss rates of infected cells of 1.04 ($CI_{95\%}$ [0.79; 1.37]) day^{-1} , corresponding to a mean half-life of 0.67 day. This estimation was consistent with previously published results obtained on SARS-CoV-2 virus showing the mean value of this parameter ranging from 0.60 to 2 days^{-1} (i.e., half-life between 0.35 and 1.16 days) (26–30). The eclipse phase (3 days^{-1}) was found similar to the values commonly used in the literature (26, 30, 32, 41). Here, we distinguished the clearance of the inoculum which was much higher (20 virions day^{-1}) as compared to the clearance of the virus produced de novo (3 virions day^{-1}). While the half-life of the virus de novo produced usually approximates 1.7 hours (i.e., $c=10 \text{ day}^{-1}$) (26, 28, 30, 32), because of this distinction, our model provided a higher estimation of 5.5 hours which remained in accordance with the estimations obtained by Baccam et al. (2006) (41) on influenza A. Furthermore, the viral production by each infected cells was estimated to be higher in the nasopharyngeal compartment (12.1×10^3 virions/cell/day, $CI_{95\%}$ [3.15×10^3 ; 46.5×10^3]) as compared to the tracheal compartment (0.92×10^3 virions/cell/day, $CI_{95\%}$ [0.39×10^3 ; 2.13×10^3]). These estimations are in agreement with the observation of the intense production of viral particles by primary human bronchial epithelial cells in culture (44). In particular, they are in the range of estimates obtained within the URT, either in NHP (28) or in humans (29), with the product pxT_0 equals to 15.1×10^8 ($CI_{95\%}$ [3.98×10^8 ; 58.1×10^8]) and 0.21×10^8 ($CI_{95\%}$ [0.088×10^8 ; 0.48×10^8]) virions/ml/day in the nasopharynx and the trachea, respectively. By allowing parameters to differ between animals (through random effects), the variation of cell infectivity and of the loss rate of infected cells captured the observed variation of the dynamics of viral load. The variation of those parameters could be partly explained by the group to which the animals belong reducing the unexplained variability of the cell infectivity by 66% and of the loss rate of infected cells by 54%

(Supplementary file 1). The model fitted well the observed dynamics of gRNA and sgRNA (Figure 2B).

Modelling of the dynamics of viral replication argues for the capacity of α CD40.RBD vaccine to block virus entry into host cells and to promote the destruction of infected cells

We distinguish the respective contribution of the vaccine effect and post-infection immunity on the reduction of the cell infection rate and the increase of the clearance of infected cells. Because blocking *de novo* infection and promoting the destruction of infected cells would lead to different viral dynamics profile (Figure 2 – figure supplement 1), we were able to identify the contribution of each mechanism by estimating the influence of the vaccine compared to placebo or naïve animals on each model parameter. The α CD40.RBD vaccine reduced by 99.6% the infection of target cells in the trachea compared to the naïve group. The estimated clearance of infected cells was 1.04 day^{-1} (95% CI 0.75; 1.45) in naïve macaques. It was increased by 80% ($1.86/\text{day}^{-1}$) in the convalescent macaques vaccinated by α CD40.RBD or not.

The mechanistic model allows predicting the dynamics of unobserved compartments. Hence, a very early decrease of the target cells (all cells expressing ACE2) as well as of the viral inoculum which fully disappeared from day 2 onward were predicted (Figure 2C). In the three groups, the number of infected cells as well as infectious viral particles increased up to day 2 and then decreased. We show that this viral dynamic was blunted in the vaccinated animals leading to a predicted maximum number of infectious viral particles in the nasopharynx and the trachea below the detection threshold (Figure 2C). The number of target cells would be decreased by the infection in the naïve and the convalescent groups, whereas it would be preserved in vaccinated animals.

The RBD-ACE2 binding inhibition is the main mechanistic CoP explaining the effect of the α CD40.RBD vaccine on new cell infection

In our study (36), an extensive evaluation of the immunological response has been performed with quantification of spike binding antibodies, antibodies inhibiting the attachment of RBD to ACE2, antibodies neutralizing infection, SARS-CoV-2-specific CD4⁺ and CD8⁺ T cells producing cytokines and serum cytokine levels (**Figure 3, Figure 1 - figure supplement 3, 4, 5**). Therefore, based on our mechanistic model we investigated if any of these markers could serve as a mechanistic CoP. Such a CoP should be able to capture the effect of the natural immunity following infection, associated or not to the vaccine (group effect) estimated on both the rate of cell infection and the rate of the loss of infected cells. To this aim, we performed a systematic screening by adjusting the model for each marker and we compared these new models with the model without covariates and with the model adjusted for the groups. In particular, our approach allowed us to benefit from all the information provided by the overall dynamics of the immunological markers after the exposure by integrating them as time-varying covariates (see the methods section for a detailed description of the algorithm). We demonstrate that the RBD-ACE2 binding inhibition measure is sufficient to capture most of the effect of the groups on the infection of target cells (**Figure 4A, 4B**). The integration of this marker in the model explains the variability of the cell infection rate with greater certainty than the group of intervention, reducing the unexplained variability by 87% compared to 66% (**Supplementary file 1**). The marker actually takes into account the variation between animals within the same group. Hence, it suggests that the levels of anti-RBD antibodies induced by the vaccine that block attachment to ACE2 are highly efficient at reflecting the neutralization of new infections *in vivo*. Furthermore, when taking into account the information provided by the RBD-ACE2 binding inhibition assay, the effect of the group of intervention was no longer significant (**Supplementary file 1**). Finally,

we looked at the estimated viral infectivity according to the binding inhibition assay in each animal. A positive dependence was found between the viral infectivity and the RBD-ACE2 binding inhibition measure, linking an increase of 10^3 AU of the marker, whether over time or between animals, with an increase of 1.8% (95CI% [1.2%; 2.3%]) of the viral infectivity (see **Supplementary file 4**). Accordingly, the values at the time of exposure were not overlapping at all, distinguishing clearly the vaccinated and unvaccinated animals (see **Figure 4C**).

In the next step, several markers (IgG binding anti-RBD antibodies, $CD8^+$ T cells producing IFN- γ) appeared to be associated to the rate of loss of infected cells (**Figure 4 – figure supplement 1A**). Both specific antibodies and specific $CD8^+$ T cells are mechanisms commonly considered important for killing infected cells. We retained the anti-RBD binding IgG Ab that were positively associated to the increase of the loss of infected cells. For unknown reason the IFN- γ response was high in unstimulated conditions in the naïve group. Thus, although this marker was associated with a decrease of the loss rate of infected cells, it appears essentially here as an indicator of the animal group. Further studies would be needed to fully confirm the place of IFN- γ response as a mechanistic marker.

A large part of the variation of the infection rate (71%) and loss rate of infected cells (60%) were captured by the two markers of CoP: the RBD-ACE2 binding inhibition and the anti-RBD binding Ab concentration. Using the estimated parameters, the effective reproduction number could be calculated (R) which is representing the number of cells secondarily infected by virus from one infected cell (**Figure 4D**). When looking at this effective reproduction number according to the groups, the vaccinated animal presented from the first day of challenge an effective R below 1 meaning that no propagation of the infection started within the host. These results were consistent when taking the value of RBD-ACE2 binding inhibition at the time of the

challenge without considering the evolution of the inhibition capacity over time (**Figure 4 - figure supplement 1B**). This means that the dynamics of the viral replication is impacted very early during the infection process in immunized (i.e., both convalescent and vaccinated) animals and that vaccinated animals were protected from the beginning by the humoral response. Then, we looked at the threshold of the markers of interest leading to the control of the within-host infection (as defined by $R < 1$) which was around 30 000 AU for the RBD-ACE2 binding inhibition assay. For the animals in the naive and the convalescent groups, the observed values of binding inhibition measured by ECL RBD (the lower the better) and of IgG anti-RBD binding antibodies (the higher the better) led to $R > 1$, whereas in vaccinated animals, the value of ECL RBD led to $R < 1$. Therefore, our modeling study shows that the inhibition of binding of RBD to ACE2 by antibodies is sufficient to control initial infection of the host (**Figure 4E**). According to the observed value of ECL RBD in vaccinated animals (e.g., 66 AU in **Figure 4E**), a decrease of more than $2 \log_{10}$ of the inhibition capacity (to reach 81 000 AU), due to variant of concern (VoC) or waning of immunity, would have been necessary to impair the control of the within-host infection. Moreover, a decrease of the neutralizing activity (i.e., increased ECL) could be compensated by an increase of cell death as measured by an increase of binding IgG anti-RBD as a surrogate. As an example, increasing IgG anti-RBD from 2.5 to 10 in the animal MF7 of the convalescent group would lead to a control of the infection.

In conclusion, the α CD40.RBD vaccine-elicited humoral response leads to the blockade of new cell infection that is well captured by measure of the inhibition of attachment of the virus to ACE2 through the RBD domain of the spike protein. Hence, the inhibition of binding of RBD to ACE2 is a promising mechanistic CoP. Indeed, this CoP fulfils the three criteria of leading to the best fit (lower BIC), the best explanation of inter-individual variability, and fully captured the effect of the group of intervention.

The model revealed the same CoP related to another protein-based vaccine but not with mRNA-1273 vaccine

We took the opportunity of another study testing a two-component spike nanoparticle protein-based vaccine performed in the same laboratory and using the same immune and virological assays (45), measured only at the time of exposure, for applying the proposed model and methodology. In this study, 6 animals were vaccinated and compared to 4 naive animals (**Figure 5A, 5B**). The good fit of the data (**Figure 5C, 5D**) allows for estimating the effect of the vaccine that appeared here also to decrease the infectivity rate (by 99%) and increase the clearance of the infected cells by 79%. Looking at the best mechanistic CoP following the previously described strategy, we ended here again with the inhibition of RBD binding to ACE2 as measured by ECL RBD. In fact, this marker measured at baseline before challenge fulfilled the three criteria: i) it led to the best model in front of a model adjusted for group effect, ii) it rendered the group effect non-significant and iii) it explained around 71% of the infectivity rate variability, compared to 65% of variability explained by the groups. Interestingly, here again, the inhibition assay led to a clear separation of the estimated rate of infectivity between vaccinees and the placebo group (**Figure 5E**).

Finally, we applied our approach to a published NHP study performed to evaluate several doses of mRNA-1273 vaccine (24). Using available data, we compared the viral dynamics in the 100 µg, 10 µg and placebo groups, enrolling a total of 12 rhesus macaques in a 1:1:1 ratio. Similar to the previous study, only immune markers measured at the time of exposure were available in this study, in addition to viral dynamics. We started from the same model as defined previously. We estimated a reduction of the infection rate by 97% but we did not find any additional effect. Looking at potential mechanistic CoP, we retained neutralization as measured on live cells with

Luciferase marker. Although this marker led to the best fit and replaced the group effect (which was non-significant after adjustment for the marker), it explained only 15% of the variability of estimated viral infectivity, while 19% were explained by the groups.

In conclusion, we demonstrated, based upon challenge studies in NHP vaccinated with two different protein-based vaccine platforms that both vaccines lead to the blockade of new cell infection. Neutralizing antibodies likely represent a consistent mechanistic correlate of protection. This could change across vaccine platforms especially because mechanisms of action are different.

DISCUSSION

We explored the mechanistic effects of three SARS-CoV-2 vaccines and assessed the quality of markers as mechanistic CoP (mCoP). This model showed that neutralizing and binding antibodies, elicited by a non-adjuvanted protein-based vaccine targeting the RBD of spike to the CD40 receptor of antigen presenting cells are reliable mCoP. Interestingly, we found the simpler and easier to standardize and implement binding inhibition assay may be more relevant to use as a correlate of protection than cell-culture neutralization assays. This result has been replicated in another study testing a nanoparticle spike vaccine. The model was able to capture the effect of the vaccines on the reduction of the rate of infection of target cells and identified additional effects of vaccines beyond neutralizing antibodies. This latter consisted of increasing the loss rate of infected cells which was better reflected by the IgG binding antibodies and CD8⁺ T cell responses in the case of the CD40-targeting vaccine. One limitation of our study is that the prediction potential of our model relies on the range of the immune markers measured. However, our approach would allow a full exploitation of the data generated as in systems serology where non-

neutralizing Ab functions, such as Ab-dependent cellular cytotoxicity (ADCC), Ab-dependent cellular phagocytosis (ADCP), Ab-dependent complement deposition (ADCD), and Ab-dependent respiratory burst (ADRB) are explored (46). The role of ADCC in natural infection has been previously shown (47), ADCD in DNA vaccine recipients (11) and with Ad26 vaccine (48). Here, we extended significantly these data by modelling the viral dynamic, showing that two other protein-based vaccines exert an additional effect on infected cell death which relied on the level of IgG anti-RBD binding antibodies especially for the CD40.RBD targeting vaccine. Measurements of other non-neutralizing Ab functions would probably also capture this additional effect.

The next question after determining which marker is a valid mCoP is to define the concentration that leads to protection, looking for a threshold effect that will help to define an objective (10, 49). In the context of SARS-CoV-2 virus, several emerged variants are leading to a significant reduction of viral neutralization as measured by various approaches. However, a 20-fold reduction of viral neutralization might not translate in 20-fold reduction of vaccine efficacy (50). First, there are many steps between viral neutralization and the reduction of viral infectivity or the improvement of clinical symptoms. Second, the consequences of a reduction of viral neutralization could be alleviated by other immunological mechanisms not compromised by the variant. In the context of natural immunity, when the level of neutralizing antibodies was below a protective threshold, the cellular immune response appeared to be critical (17, 51). We showed with our model that an improvement of infected cell destruction could help to control the within-host infection and is quantitatively feasible.

The control of viral replication is the key for reducing infectivity (52, 53) as well as disease severity (54, 55). According to our non-linear model linking the neutralization to the viral

replication, a decrease of 4 to 20-fold in neutralization as described for the variants of concern (4, 6) is not enough, especially in the context of the response to CD40.RBD targeting vaccine, to compromise the control of viral replication. The results showing a conserved effectiveness of mRNA vaccines in humans infected by the alpha or beta variants (56), although a decrease of neutralization has been reported (4), are consistent with this hypothesis. However, this is highly dependent upon the mode of action of currently used vaccines and upon the VoC that may much more compromise the neutralization but being also intrinsically less pathogenic such as Omicron (57).

The analysis performed extended significantly the observation of associations between markers as previously reported for SARS-CoV-2 vaccine (11) and other vaccines (58) because it allows a more causal interpretation of the effect of immune markers. However, our modelling approach requires the *in vivo* identification of the biological parameters under specific experimentations. On the other hand, the estimation of parameters included in our model also provided information on some aspect of the virus pathophysiology. Notably, we found an increased capacity of virion production in nasopharynx compared to the trachea which could be explained by the difference in target cells according to the compartment (59). This result needs to be confirmed as it may also be the consequence of a different local immune response (60). The choice of the structural model defining the host-pathogen interaction is a fundamental step in the presented approach. Here, it was well guided by the biological knowledge, the existing models for viral dynamics (34, 61, 62) and the statistical inference allowing the selection of the model that best fit the data. As the number of observations was relatively small in regard to the number of model parameters, we investigated overfitting issues. This was done using a bootstrap approach to evaluate the stability of confidence intervals of the estimated parameters. Results are provided in Appendix 2 “BICc as

selection criteria and multiple testing adjustment”. Many modeling choices for the statistical model were made in this approach and more theoretical work evaluating the robustness of the results in their regards may be relevant for future works. In particular, we could relax the constraint of linear interpolation of marker dynamics by using simple regression models, allowing in the same time the integration of error model to account for measurement error for time-varying covariates (63–65). Moreover, by construction, we assumed similar interindividual variability and effects of covariates within the two URT compartments as well as similar values for the viral infectivity and the loss rate of infected cells. Viral load dynamics measured in lungs being different from those in the URT (66, 67), the relaxation of this hypothesis of homogeneous physiological behavior in the URT may be pertinent to extend the model to the LRT. Finally, it should be underlined that the dynamics of the immune response has not been modelled as suggested for instance for B cell response (68). This clearly constitutes the next step after the selection of the markers of interest as done in the present work.

In conclusion, the modelling of the response to two new promising SARS-CoV-2 vaccines in NHP revealed a combination of effects with a blockade of new cell infections and the destruction of infected cells. For these two vaccines, the antibody inhibiting the attachment of RBD to ACE2, appeared to be a very good surrogate of the vaccine effect on the rate of infection of new cells and therefore could be used as a mechanistic CoP. This modelling framework contributes to the improvement of the understanding of the immunological concepts by adding a quantitative evaluation of the contributions of different mechanisms of control of viral infection. In terms of acceleration of vaccine development, our results may help to develop vaccines for “hard-to-target pathogens”, or to predict their efficacy in aging and particular populations (69). It should also help in choosing vaccine dose, for instance at early development (70) as well as deciding if and

when boosting vaccination is needed in the face of waning protective antibody levels (71, 72), at least in NHP studies although the framework could be extended to human studies using mixed approaches of within and between hosts modelling (73) providing that enough information is collected.

MATERIALS AND METHODS

Experimental model and subjects details

Cynomolgus macaques (*Macaca fascicularis*), aged 37-66 months (18 females and 13 males) and originating from Mauritian AAALAC certified breeding centers were used in this study. All animals were housed in IDMIT facilities (CEA, Fontenay-aux-roses), under BSL2 and BSL-3 containment when necessary (Animal facility authorization #D92-032-02, Préfecture des Hauts de Seine, France) and in compliance with European Directive 2010/63/EU, the French regulations and the Standards for Human Care and Use of Laboratory Animals, of the Office for Laboratory Animal Welfare (OLAW, assurance number #A5826-01, US). The protocols were approved by the institutional ethical committee “Comité d’Ethique en Expérimentation Animale du Commissariat à l’Energie Atomique et aux Energies Alternatives” (CEtEA #44) under statement number A20-011. The study was authorized by the “Research, Innovation and Education Ministry” under registration number APAFIS#24434-2020030216532863v1.

Evaluation of anti-Spike, anti-RBD and neutralizing IgG antibodies

Anti-Spike IgG were titrated by multiplex bead assay. Briefly, Luminex beads were coupled to the Spike protein as previously described (74) and added to a Bio-Plex plate (BioRad). Beads were washed with PBS 0.05% tween using a magnetic plate washer (MAG2x program) and

incubated for 1h with serial diluted individual serum. Beads were then washed and anti-NHP IgG-PE secondary antibody (Southern Biotech, clone SB108a) was added at a 1:500 dilution for 45 min at room temperature. After washing, beads were resuspended in a reading buffer 5 min under agitation (800 rpm) on the plate shaker then read directly on a Luminex Bioplex 200 plate reader (Biorad). Average MFI from the baseline samples were used as reference value for the negative control. Amount of anti-Spike IgG was reported as the MFI signal divided by the mean signal for the negative controls.

Anti-RBD and anti-Nucleocapside (N) IgG were titrated using a commercially available multiplexed immunoassay developed by Mesoscale Discovery (MSD, Rockville, MD) as previously described (75). Briefly, antigens were spotted at 200–400 µg/mL in a proprietary buffer, washed, dried and packaged for further use (MSD® Coronavirus Plate 2). Then, plates were blocked with MSD Blocker A following which reference standard, controls and samples diluted 1:500 and 1:5000 in diluent buffer were added. After incubation, detection antibody was added (MSD SULFO-TAG™ Anti-Human IgG Antibody) and then MSD GOLD™ Read Buffer B was added and plates read using a MESO QuickPlex SQ 120MM Reader. Results were expressed as arbitrary unit (AU)/mL.

Anti-RBD and anti-N IgG were titrated by ELISA. The Nucleocapsid and the Spike RBD domain (Genbank # NC_045512.2) were cloned and produced in *E. Coli* and CHO cells, respectively, as previously described (37). Antigens were purified on C-tag column (Thermo Fisher) and quality-controlled by SDS-PAGE and for their level of endotoxin. Antigens were coated in a 96 wells plates Nunc-immuno Maxisorp (Thermo Fisher) at 1 µg/mL in carbonate buffer at 4°C overnight. Plates were washed in TBS tween 0.05% (Thermo Fisher) and blocked with PBS 3% BSA for 2

hours at room temperature. Samples were then added, in duplicate, in serial dilution for 1 hour at RT. Non-infected NHP sera were used as negative controls. After washing, anti-NHP IgG coupled with HRP (Thermo Fisher) was added at 1:20,000 for 45 min at RT. After washing, TMB substrate (Thermo Fisher) was added for 15 min at RT and the reaction was stopped with 1M sulfuric acid. Absorbance of each well was measured at 450 nm (reference 570 nm) using a Tristar2 reader (Berthold Technologies). The EC_{50} value of each sample was determined using GraphPad Prism 8 and antibody titer was calculated as $\log(1/EC_{50})$.

The MSD pseudo-neutralization assay was used to measure antibodies neutralizing the binding of the spike protein to the ACE2 receptor. Plates were blocked and washed as above, assay calibrator (COVID- 19 neutralizing antibody; monoclonal antibody against S protein; 200 $\mu\text{g/mL}$), control sera and test sera samples diluted 1:10 and 1:100 in assay diluent were added to the plates. Following incubation of the plates, an 0.25 $\mu\text{g/mL}$ solution of MSD SULFO-TAGTM conjugated ACE-2 was added after which plates were read as above. Electro-chemiluminescence (ECL) signal was recorded.

Viral dynamics modelling

The mechanistic approach we developed to characterize the impact of the immune response on the viral gRNA and sgRNA dynamics relies on a mechanistic model divided in three layers: firstly, we used a mathematical model based on ordinary differential equations to describe the dynamics in the two compartments, the nasopharynx and the trachea. Then we used a statistical model to take into account both the inter-individual variability and the effects of covariates on parameters. Finally, we considered an observation model to describe the observed \log_{10} viral loads in the two compartments.

452 For the mathematical model, we started from previously published models (26, 27, 41) where the
 453 nasopharynx and trachea were respectively described by a target cell limited model, with an
 454 eclipse phase, as model of acute viral infection assuming target-cell limitation (33). We
 455 completed the model by adding a compartment for the inoculum that distinguishes the injected
 456 virus (V_s) from the virus produced *de novo* (V_i and V_{ni}). To our knowledge, this distinction has
 457 not been proposed in any previous work. Two main reasons led us to make this choice. First, it
 458 allowed us to study the dynamics of the inoculum, in particular during the early phase of viral
 459 RNA load dynamics. Second, as described in more detail below, it gave us the opportunity to use
 460 all the information provided by the preclinical studies, such as the known number of inoculated
 461 virions, to define the initial conditions of the ODE model rather than estimating or randomly
 462 fixing them for V_i and V_{ni} , as is usually done. Consequently, for each of the two compartments,
 463 the model included uninfected target cells (T) that can be infected (I_1) either by infectious viruses
 464 (V_i) or inoculum (V_s) at an infection rate β . After an eclipse phase, infected cells become
 465 productively infected cells (I_2) and can produce virions at rate P and be lost at a per capita rate δ .
 466 The virions generated can be infectious (V_i) with proportion μ while the $(1-\mu)$ remaining
 467 proportion of virions is non-infectious (V_{ni}). Mathematically, a single compartment (V) for *de*
 468 *nov*o produced virions could be considered in the model, with μV and $(1-\mu)V$ representing the
 469 respective contributions of infectious and non-infectious viruses to the biological mechanisms.
 470 However, to have a better visual understanding of the distinction between the two types of
 471 viruses, we wrote the model with distinct compartments, V_i and V_{ni} .
 472 Finally, virions produced *de novo* and those from the inoculum are cleared at a rate c and c_i
 473 respectively. Distinct clearances were considered to account for the effects of experimental
 474 conditions on viral dynamics. In particular, it is hypothesized that, animals being locally infected

475 with large numbers of virions, a large proportion of it is assumed to be rapidly eliminated by
 476 swallowing and natural downstream influx, in contrast to the *de novo* produced virions. However,
 477 it is important to keep in mind that this distinction was possible because of the controlled
 478 experimental conditions performed in animals, (i.e., exact timing and amount of inoculated virus
 479 known, and frequent monitoring during the early phase of the viral dynamics). Because of
 480 identifiability issues, similar clearances for infectious and non-infectious viruses were used.
 481 Accordingly, the model can be written as the following set of differential equations, where the
 482 superscript X denotes the compartment of interest (N, nasopharynx or T, trachea):

$$\left\{ \begin{array}{l} \frac{dT^X}{dt} = -\beta^X V_i^X T^X - \mu \beta^X V_s^X T^X \\ \frac{dI_1^X}{dt} = \beta^X V_i^X T^X + \mu \beta^X V_s^X T^X - k I_1^X \\ \frac{dI_2^X}{dt} = k I_1^X - \delta^X I_2^X \\ \frac{dV_i^X}{dt} = \mu P^X I_2^X - c V_i^X - \beta^X V_i^X T^X \\ \frac{dV_{ni}^X}{dt} = (1 - \mu) P^X I_2^X - c V_{ni}^X \\ \frac{dV_s^X}{dt} = -c_i V_s^X - \mu \beta^X V_s^X T^X \\ T^X(t=0) = T_0^X ; I_1^X(t=0) = 0 ; I_2^X(t=0) = 0 \\ V_i^X(t=0) = 0 ; V_{ni}^X(t=0) = 0 ; V_s^X(t=0) = V_{s,0}^X \end{array} \right. \quad \# \quad (1)$$

483 where $T^X(t=0)$, $I_1^X(t=0)$, $I_2^X(t=0)$, $V_i^X(t=0)$, $V_{ni}^X(t=0)$ and $V_s^X(t=0)$ are the initial
 484 conditions at the time of exposure. The initial concentration of target cells, that are the epithelial
 485 cells expressing the ACE2 receptor, is expressed as $T_0^X = \frac{T_0^{X,nbc}}{W^X}$ where $T_0^{X,nbc}$ is the initial
 486 number of cells and W^X is the volume of distribution of the compartment of interest (see the
 487 subsection “Consideration of the volume of distribution”). Each animal was exposed to 1×10^6 pfu
 488 of SARS-CoV-2 representing a total of 2.19×10^{10} virions. Over the total inoculum injected (5

mL), 10% (0.5 mL) and 90% (4.5 mL) of virions were respectively injected by the intra-nasal route and the intra-tracheal route leading to the following initial concentrations of the inoculum within each compartment : $V_{S,0}^N = \frac{0.10 \times \text{Inoc}_0}{W^N}$ and $V_{S,0}^T = \frac{0.90 \times \text{Inoc}_0}{W^T}$, with Inoc_0 the number of virions injected via the inoculum.

Using the gRNA and sgRNA viral loads, we estimated the viral infectivity, the viral production rate and the loss rate of infected cells within each of the two compartments of the URT (**Supplementary file 2**). To account for inter-individual variability and covariates, each of those three parameters was described by a mixed-effect model and jointly estimated between the two compartments as follows:

$$\begin{cases} \log_{10}(\beta_i^N) = \beta_0 + \phi_{conv}^\beta \times \mathbb{I}_{group=conv} + \phi_{CD40}^\beta \times \mathbb{I}_{group=CD40} + u_i^\beta \\ \beta_i^T = \beta_i^N \times \exp(f_\beta^T) \\ \log(\delta_i^N) = \log(\delta_0) + \phi_{conv}^\delta \times \mathbb{I}_{group=conv} + \phi_{CD40}^\delta \times \mathbb{I}_{group=CD40} + u_i^\delta \\ \delta_i^T = \delta_i^N \times \exp(f_\delta^T) \\ \log(P_i^N) = \log(P_0) + \phi_{conv}^P \times \mathbb{I}_{group=conv} + \phi_{CD40}^P \times \mathbb{I}_{group=CD40} + u_i^P \\ P_i^T = P_i^N \times \exp(f_P^T) \end{cases} \quad (2)$$

where $\beta_0, \log(\delta_0)$ and $\log(P_0)$ are the fixed effects, $\{\phi_{conv}^\theta | \theta \in \{\beta, \delta, P\}\}$ and $\{\phi_{CD40}^\theta | \theta \in \{\beta, \delta, P\}\}$ are respectively the regression coefficients related to the effects of the group of convalescent and α CD40.RBD vaccinated animals for the parameters β , δ and P , and u_i^θ is the individual random effect for the parameter θ , which is assumed to be normally distributed with variance ω_θ^2 . A log-transformation was adopted for the parameters δ and P to ensure their positivity while a \log_{10} -transformation was chosen for viral infectivity to also improve the convergence of the estimation. Because of the scale difference between the parameter β and the other parameters (see **Supplementary file 2**), the mere use of the log-transformation for this parameter led to convergence issues. The use of a \log_{10} -transformation allowed to overcome this

problem. Moreover, as shown in Equation (2), a joint estimation of the parameters β , δ and P between the two compartments of the URT was considered. In this regard, a homogeneous interindividual variability within the URT was assumed as well as a similar contribution of the covariates to the value of the parameters. Parameters in the trachea were then either equal or proportional to those in the nasopharynx. This modeling choice, resulting in a smaller number of parameters to be estimated, was made mainly to address identifiability issues and to increase the power of the estimation. All other parameters included in the target-cell limited models were assumed to be fixed (see the subsection “Parameter estimation” for more details).

In practice, after the selection of the optimal statistical model (see Appendix 1 “Model Building”), random effects were added only to the parameters β and δ (i.e., $\omega_\beta \neq 0$, $\omega_\delta \neq 0$, and $\omega_P=0$), and the estimation of multiple models identified the viral production rate P as the only parameter taking different values between the trachea and nasopharynx. (i.e., $\beta^N=\beta^T$ with $f_\beta^T=0$, $\delta^N=\delta^T$ with $f_\delta^T=0$, while $P^N \neq P^T$). Finally, the adjustment of the model for the categorical covariates of groups of treatment, natural infection and/or vaccination, identified β and δ as the parameters with a statistically significant effect of these covariates (i.e., $\phi_{conv}^P = 0$ and $\phi_{CD40}^P = 0$).

For the observation model, we jointly described genomic and subgenomic viral loads in the two compartments of the URT. We defined genomic viral load, which characterizes the total viral load observed in a compartment (nasopharynx or trachea), as the sum of inoculated virions (V_s), infectious (V_i) and non-infectious virions (V_{ni}). The sgRNA was described as proportional to the infected cells ($I_1 + I_2$). This choice was driven by two main reasons. First, sgRNA is only transcribed in infected cells (76). Second, as described by Miao et al. (2011) (77), to overcome identifiability issues between the parameters β and P typically observed in target-cell limited

models. The comparison of the two observation models describing sgRNA as either proportional to virions produced *de novo* ($V_i + V_{ni}$) or proportional to infected cells ($I_1 + I_2$) confirmed this conclusion. In addition to a better BICc value (-25 points) compared with the first model, the second one allowed the estimation of both β and P by counteracting identifiability problems faced with the first model (results not shown). Accordingly, the \log_{10} -transformed gRNA and sgRNA of the i th animal at the j th time point in compartment X (nasopharynx or trachea), denoted $gRNA_{ij}^X$ and $sgRNA_{ij}^X$ respectively, were described by the following equations:

$$\begin{cases} gRNA_{ij}^X = \log_{10}[V_i^X + V_{ni}^X + V_s^X](\Theta_i^X, t_{ij}) + \varepsilon_{ij,g}^X & \varepsilon_{ij,g}^X \sim \mathcal{N}(0, \sigma_{gX}^2) \\ sgRNA_{ij}^X = \alpha_{sgRNA} \times \log_{10}[I_1^X + I_2^X](\Theta_i^X, t_{ij}) + \varepsilon_{ij,sg}^X & \varepsilon_{ij,sg}^X \sim \mathcal{N}(0, \sigma_{sgX}^2) \end{cases} \quad (3)$$

where Θ_i^X is the set of parameters of the subject i for the compartment X and ε are the additive normally distributed measurement errors.

Consideration of the volume of distribution

To define the concentration of inoculum within each compartment after injection, nasopharyngeal and tracheal volumes of distribution, labelled W^N and W^T respectively, were needed. Given the estimated volumes of the trachea and the nasal cavities in four monkeys similar to our 18 macaques (**Figure 2 - figure supplement 2A-C**) and the well documented relationship between the volume of respiratory tract and animal weights (78), the volume of distribution of each compartment was defined as a step function of NHP weights:

$$\begin{aligned} W_i^N &= \begin{cases} 4 & \text{if Weight}_i \leq 4.5 \\ 5.5 & \text{otherwise} \end{cases} \\ W_i^T &= \begin{cases} 2 & \text{if Weight}_i \leq 4.5 \\ 3 & \text{otherwise} \end{cases} \end{aligned} \quad (4)$$

Where Weight_i is the weight of the monkey i in kgs. Using equation (4) and weights of our 18 NHPs (mean= 4.08 ; [Q1 ; Q3] = [3.26 ; 4.77]), we estimated $W^T = 2$ and $W^N = 4\text{mL}$ for a third

of them ($n=12$) (**Figure 2 - figure supplement 2D**), leading to the initial concentration of target cells T_0^X (see “Viral dynamics modeling” for equation) fixed at 3.13×10^4 cells.mL⁻¹ and 1.13×10^4 cells.mL⁻¹ in nasopharynx and trachea respectively. Similarly, their initial concentrations of challenge inoculum $V_{S,0}^X$ were fixed at 5.48×10^8 copies.mL⁻¹ and 9.86×10^9 copies.mL⁻¹ in nasopharynx and trachea resp. For the last third of NHPs ($n=6$), $W^T = 3$ and $W^N = 5.5$ mL leading to T_0^X fixed at 2.27×10^4 cells.mL⁻¹ in nasopharynx and 7.50×10^3 cells.mL⁻¹ in trachea while $V_{S,0}^X$ was fixed at 3.98×10^8 copies.mL⁻¹ in nasopharynx and 6.57×10^9 copies.mL⁻¹ in trachea. Through this modeling, we assumed a homogenous distribution of injected virions and target cells within nasopharyngeal and tracheal compartments. In addition, the natural downward flow of inoculum towards lungs, at the moment of injection, was indirectly taken into account by the parameter of inoculum clearance, c_i .

Parameter estimation

Among all parameters involved in the three layers of the mechanistic model, some of them have been fixed based on experimental settings and/or literature. That is the case of the proportion of infectious virus (μ) that has been fixed at 1/1000 according to previous work (28) and additional work (results not shown) evaluating the stability of the model estimation according to the value of this parameter. The initial number of target cells, that are the epithelial cells expressing the ACE2 receptor, $T_0^{X,nbc}$ was fixed at 1.25×10^5 cells in the nasopharynx and 2.25×10^4 cells in trachea (28) (**Supplementary file 2**). The duration of the eclipse phase ($1/k$), the clearance of the inoculum (c_i) and the clearance of the virus produced *de novo* (c) were estimated by profile likelihood. The profile likelihood consists in defining a grid of values for the parameters to be evaluated and sequentially fixing these parameters to one of these combinations of values. The

model and all the parameters that are not fixed are then estimated by maximizing the log-likelihood. In this process, all parameters that are assumed to be fixed in the model (i.e., μ and the initial conditions) are held fixed. Finally, the optimal set of parameters is chosen as the one optimizing the log-likelihood. Although the available data did not allow the direct estimation of these three parameters, the use profile likelihood enabled the exploration of various potential values for k , c and c_i . In a first step, we explored the 18 models resulting from the combination of 3 values of $k \in \{1, 3, 6\} \text{ day}^{-1}$ and 6 values for $c \in \{1, 5, 10, 15, 20, 30\} \text{ day}^{-1}$, assuming that the two parameters of virus clearance were equal, as first approximation. As shown in **Supplementary file 3a**, an eclipse phase of 8 hours ($k=3$) and virus clearance higher than 15 virions per day led to lowest values of -2log-likelihood (-2LL, the lower the better). In a second step, we fixed the parameter k at 3 day^{-1} and estimated the 70 models resulting from the combination of 10 values for $c \in \{1, 2, 3, 4, 5, 10, 15, 20, 25, 30\} \text{ day}^{-1}$ and 7 values for $c_i \in \{1, 5, 10, 15, 20, 25, 30\} \text{ day}^{-1}$ (**Supplementary file 3b**). The distinction of the two parameters of free virus clearance enabled to find much lower half-life of inoculum (~ 50 minutes) than half-life of virus produced *de novo* (~ 5.55 hours), with $c=3 \text{ day}^{-1}$ compared to $c_i=20 \text{ day}^{-1}$.

Once all these parameters have been fixed, the estimation problem was restricted to the determination of the viral infectivity β , the viral production rate P , the loss rate of infected cells δ for each compartment, the parameter α_{vlsq} in the observation model, regression coefficients for groups of intervention (ϕ_{conv} , ϕ_{DC40}) and standard deviations for both random effects (ω) and error model (σ). The estimation was performed by Maximum likelihood estimation using a stochastic approximation EM algorithm implemented in the software Monolix (<http://www.lixoft.com>). The Fisher Information Matrix (FIM) was calculated by stochastic

approximation, providing for each estimated parameter its variance, from which we were able to derive its 95% confidence interval. Selection of the compartment effect on parameters (β , δ , P) as well as random effects and covariates on the statistical model (2) was performed by the estimation of several models that were successively compared according to the corrected Bayesian information criterion (BICc) (to be minimized). After the removal of random effect on the viral production ($\omega_P = 0$) allowing the reduction of the variance on the two other random effects, all combinations of compartment effects were evaluated, leading to the final selection of a single effect on P ($f_\beta^T = f_\delta^T = 0$). Then, the effect of group intervention was independently added on model parameters among β , δ , P and c . Once the group effect on the viral infectivity identified as the best one, the addition of a second effect on the remaining parameters was tested, resulting in the selection of the loss rate of infected cells. Finally, the irrelevance of the addition of a third effect was verified.

The possibility of migration of free plasma virus between the nasopharynx and the trachea was tested. However, as widely described in the literature, the transport of viral particles within the respiratory tract is negligible in the viral dynamics and is difficult to estimate. The reader can refer to Appendix 1 “Model building” for an additional modelling work conducted to estimate this exchange and provided the same conclusion. Accordingly, the two compartments of the URT were assumed are distinct in our model.

Algorithm for automatic selection of biomarkers as CoP

After identifying the effect of the group of intervention on both the viral infectivity (β) and the loss rate of infected cells (δ), we aimed at determining whether some immunological markers quantified in the study could capture this effect. Nowadays, many methods for selecting constant covariates already exist (80) and are implemented in software like Monolix. However, these latter do not allow time-varying covariates. In this section, we present the algorithm we implemented to select time-varying covariates. We proposed a classical stepwise data-driven automatic covariate modelling method (**Figure 4 - figure supplement 2**). However, initially implemented to select covariates from more than 50 biomarkers, computational time restricted us to consider only a forward selection procedure. Nevertheless, the method can be easily extended to classical stepwise selection in which both forward selection and backward elimination are performed sequentially. Although the method was developed for time-varying covariates, it can also be applied to constant covariates.

At the initialization step ($k=0$) (see **Figure 4 – figure supplement 2**), the algorithm requests 3 inputs: (1) a set of potential M covariates, labelled Marker_m for $m \in \{1, \dots, M\}$ (e.g., immunological markers) ; (2) a set of P parameters on which covariates could be added, labelled θ_p for $p \in \{1, \dots, P\}$ (e.g. β and δ) ; and (3) an initial model (e.g., the model without covariates), labelled M^0 , with θ_p^0 being the definition of the parameter θ_p . At each step $k>0$, we note M^{k-1} the current model resulting in the model built in the step $k-1$. Then each combination of markers and parameters that have not already been added in M^{k-1} , labelled r ($r \in \{\text{Marker } m \otimes \theta_p \notin M^{k-1} \mid m \in \{1, \dots, M\}, p \in \{1, \dots, P\}\}$), are considered and tested in an univariate manner (each relation r is independently added in M^{k-1} and ran). To this end, the parameter θ_p involved in this relationship r is modified as $\theta_p^k(t) = \theta_p^{k-1}(t) \times \exp(\phi_m^p \times \text{Marker}_m(t))$, where ϕ_m^p is the

regression coefficient related the marker and $Marker_m(t)$ being the trajectory of the marker over
 time, while other parameters remain unchanged ($\forall \theta_q \notin r, \theta_q^k(t) = \theta_q^{k-1}(t)$). Once all these
 models evaluated, the one with the optimal value of a given selection criterion defining the
 quality of the fits (e.g., the lowest BICc value) is selected and compared to the model M^{k-1} . If the
 value of the criterion is better than the one found for M^{k-1} , then this model is defined as the new
 current model, M^k , and the algorithm moves to the step $k+1$. Otherwise, the algorithm stops. The
 algorithm can also be stopped at the end of a fixed number of step K .
 The objective of this algorithm being to identify mechanistic correlates of protection, at each
 step, the selected model should respect, in addition to the best fits criterion, the 2 other criteria
 defining mCoP meaning the ability to capture the effect of the group of intervention and the
 ability to better explain the variability on individual parameters than the model adjusted for the
 group effect. To this end, we verify that in the selected model additionally adjusted for the group
 of intervention, the group effect appears as non-significantly different from 0 using a Wald-test.
 Then, we check that the variances of random effects in the selected model are lower or equal to
 the ones obtained in the model adjusted only for the group effect.

Modelling hypothesis for time-dependent covariates in our application

Using a population-based approach to estimate our mechanistic model and similar to the
 adjustment of the model for constant covariates (e.g., groups of intervention), time-varying
 covariates are incorporated into the statistical model as individual-specific explanatory variables
 in the mixed-effects models. To implement the algorithm for selecting the time-varying
 covariates, many modeling choices were made. First, targeting covariates able to fully replace the
 group of intervention, we kept a similar mathematical relationship between parameters and

immune markers than the one used with the constant covariate (see Equation (2)). Accordingly, we adjusted the model parameters additively in logarithmic scale. In this regard, at each step k ($k > 0$), the parameter θ_p was defined as $\log(\theta_p^k(t)) = \log(\theta_p^{k-1}(t)) + \phi_m^p \times \text{Marker}_m(t)$. However, this choice may affect the results and other choices may be more relevant under different conditions. Second, because immune markers are observed only at discrete time points, whereas the estimation of the model is performed in a continuous way, we introduced immune markers as time-varying covariates using linear interpolation. Let's denote $\text{Marker}_{i,j}$ the value of the marker observed for the i th animal at the j th time point, with $i \in \{1, \dots, n\}$ and $j \in \{1, \dots, J\}$. By linear interpolation, the time-continuous marker was defined as, $\forall t > 0$,

$$\begin{aligned} \text{Marker}_i^{\text{int}}(t) = & \sum_{j=1}^{J-1} \mathbb{I}_{[t_j; t_{j+1}[}(t) \left[\frac{\text{Marker}_{i,j+1} - \text{Marker}_{i,j}}{t_{j+1} - t_j} t + \frac{\text{Marker}_{i,j} t_{j+1} - \text{Marker}_{i,j+1} t_j}{t_{j+1} - t_j} \right] \\ & + \mathbb{I}_{t \geq t_J}(t) \times \text{Marker}_{i,J} \end{aligned}$$

As previously described in the Results section, three different studies were considered in this work: a main study reported by Marlin et al. (36) testing the α CD40.RBD vaccine, and two additional studies (24, 45) evaluating a two-component spike nanoparticle vaccine and the mRNA-1273 vaccine, respectively. In the main study, the method was applied with both time-varying covariates and constant covariates for which only baseline value was considered, such that $\text{Marker}_i(t) = \text{Marker}_i(t=0)$ (see **Supplementary file 1**). For the other two studies, only the baseline values were considered as covariates, the dynamics being not available. To assess the robustness of the results, several selection criteria were tested: AIC, BIC, log-likelihood, the percentage of explained interindividual variability, and similar results were obtained for all (results not shown). Moreover, as presented in Appendix 2 “BICc as selection criteria and

multiple testing adjustment”, we verified the robustness of the use of BIC as selection criteria despite the multiplicity of the tests. The identification of antibodies inhibiting the attachment of the RBD domain to the ACE2 receptor (ECLRBD) as the first time-varying CoP led to the definition of the time-varying viral infectivity for the i -th animal as described in Equation (5), while the selection anti-RBD IgG-binding antibodies (IggRBD) led to the elimination rate of infected cells given in Equation (6).

$$\beta_i(t) = 10^{\beta_0 + u_i^\beta} \times \exp\left(\phi_{ecl}^\beta \times ECLRBD_i^{int}(t)\right) \quad (5)$$

$$\delta_i(t) = \delta_0 \times \exp(\phi_{igg}^\delta \times IggRBD_i^{int}(t) + u_i^\delta) \quad (6)$$

Quantification and statistical analysis

In each of the three studies used in this work, no statistical tests were performed on the raw data (i.e, observations), whether for viral load or for immune marker measurements, to identify statistical differences between treatment groups, as the statistical analyses were already been performed in the respective papers. Statistical significance of the effect of groups in model estimation is indicated in the tables by stars: *, $p < 0.05$; **, $p < 0.01$; ***, $p < 0.001$ and were estimated by Wald tests (Monolix® software version 2019R1).

Model parameters were estimated with the SAEM algorithm (Monolix® software version 2019R1). Graphics were generated using R version 3.6.1 and Excel 2016 and details on the statistical analysis for the experiments can be found in the accompanying figure legends. Horizontal red dashed lines on graphs indicate assay limit of detection.

References and Notes

1. World Health Organisation, COVID-19 vaccine tracker and landscape (2021) (available at <https://www.who.int/publications/m/item/draft-landscape-of-covid-19-candidate-vaccines>).
2. S. Cobey, D. B. Larremore, Y. H. Grad, M. Lipsitch, Concerns about SARS-CoV-2 evolution should not hold back efforts to expand vaccination. *Nat Rev Immunol* **21**, 330–335 (2021).
3. A. Kuzmina, Y. Khalaila, O. Voloshin, A. Keren-Naus, L. Boehm-Cohen, Y. Raviv, Y. Shemer-Avni, E. Rosenberg, R. Taube, SARS-CoV-2 spike variants exhibit differential infectivity and neutralization resistance to convalescent or post-vaccination sera. *Cell host & microbe* **29**, 522-528.e2 (2021).
4. D. Planas, T. Bruel, L. Grzelak, F. Guivel-Benhassine, I. Staropoli, F. Porrot, C. Planchais, J. Buchrieser, M. M. Rajah, E. Bishop, M. Albert, F. Donati, M. Prot, S. Behillil, V. Enouf, M. Maquart, M. Smati-Lafarge, E. Varon, F. Schortgen, L. Yahyaoui, M. Gonzalez, J. De Sèze, H. Pérè, D. Veyer, A. Sève, E. Simon-Lorière, S. Fafi-Kremer, K. Stefic, H. Mouquet, L. Hocqueloux, S. van der Werf, T. Prazuck, O. Schwartz, Sensitivity of infectious SARS-CoV-2 B.1.1.7 and B.1.351 variants to neutralizing antibodies. *Nat Med* **27**, 917–924 (2021).
5. Y. Lustig, I. Nemet, L. Kliker, N. Zuckerman, R. Yishai, S. Alroy-Preis, E. Mendelson, M. Mandelboim, Neutralizing Response against Variants after SARS-CoV-2 Infection and One Dose of BNT162b2. *New England Journal of Medicine* **384**, 2453–2454 (2021).
6. D. Zhou, W. Dejnirattisai, P. Supasa, C. Liu, A. J. Mentzer, H. M. Ginn, Y. Zhao, H. M. E. Duyvesteyn, A. Tuekprakhon, R. Nitalai, B. Wang, G. C. Paesen, C. Lopez-Camacho, J. Slon-Campos, B. Hallis, N. Coombes, K. Bewley, S. Charlton, T. S. Walter, D. Skelly, S. F. Lumley, C. Dold, R. Levin, T. Dong, A. J. Pollard, J. C. Knight, D. Crook, T. Lambe, E. Clutterbuck, S. Bibi, A. Flaxman, M. Bittaye, S. Belij-Rammerstorfer, S. Gilbert, W. James, M. W. Carroll, P. Klennerman, E. Barnes, S. J. Dunachie, E. E. Fry, J. Mongkolsapaya, J. Ren, D. I. Stuart, G. R. Screaton, Evidence of escape of SARS-CoV-2 variant B.1.351 from natural and vaccine-induced sera. *Cell* **184**, 2348-2361.e6 (2021).
7. A. Greinacher, T. Thiele, T. E. Warkentin, K. Weisser, P. A. Kyrle, S. Eichinger, Thrombotic Thrombocytopenia after ChAdOx1 nCov-19 Vaccination. *The New England journal of medicine* **384**, 2092–2101 (2021).
8. T. Koch, S. C. Mellinghoff, P. Shamsrizi, M. M. Addo, C. Dahlke, Correlates of Vaccine-Induced Protection against SARS-CoV-2. *Vaccines* **9**, 238 (2021).
9. P. Jin, J. Li, H. Pan, Y. Wu, F. Zhu, Immunological surrogate endpoints of COVID-2019 vaccines: the evidence we have versus the evidence we need. *Signal transduction and targeted therapy* **6**, 48 (2021).
10. D. S. Khoury, D. Cromer, A. Reynaldi, T. E. Schlub, A. K. Wheatley, J. A. Juno, K. Subbarao, S. J. Kent, J. A. Triccas, M. P. Davenport, Neutralizing antibody levels are highly predictive of immune protection from symptomatic SARS-CoV-2 infection. *Nat Med* **27**, 1205–1211 (2021).
11. J. Yu, L. H. Tostanoski, L. Peter, N. B. Mercado, K. McMahan, S. H. Mahrokhian, J. P. Nkolola, J. Liu, Z. Li, A. Chandrashekar, D. R. Martinez, C. Loos, C. Atyeo, S. Fischinger, J. S. Burke, M. D. Slein, Y. Chen, A. Zuiani, F. J. N. Lelis, M. Travers, S. Habibi, L. Pessaint, A. Van Ry, K. Blade, R. Brown, A. Cook, B. Finneyfrock, A. Dodson, E. Teow, J. Velasco, R. Zahn, F. Wegmann, E. A. Bondzie, G. Dagotto, M. S. Gebre, X. He, C. Jacob-Dolan, M. Kirilova, N. Kordana, Z. Lin, L. F. Maxfield, F. Nampanya, R. Nityanandam, J. D. Ventura, H. Wan, Y. Cai, B. Chen, A. G. Schmidt, D. R. Wesemann, R. S. Baric, G. Alter, H. Andersen, M. G. Lewis, D. H. Barouch, DNA vaccine protection against SARS-CoV-2 in rhesus macaques. *Science (New York, N.Y.)* **369**, 806–811 (2020).
12. K. A. Earle, D. M. Ambrosino, A. Fiore-Gartland, D. Goldblatt, P. B. Gilbert, G. R. Siber, P. Dull, S. A. Plotkin, Evidence for antibody as a protective correlate for COVID-19 vaccines. *Vaccine* **39**, 4423–4428 (2021).

741 13. S. Feng, D. J. Phillips, T. White, H. Sayal, P. K. Aley, S. Bibi, C. Dold, M. Fuskova, S. C. Gilbert, I. Hirsch, H.
742 E. Humphries, B. Jepson, E. J. Kelly, E. Plested, K. Shoemaker, K. M. Thomas, J. Vekemans, T. L. Villafana, T.
743 Lambe, A. J. Pollard, M. Voysey, Correlates of protection against symptomatic and asymptomatic SARS-CoV-2
744 infection. *Nat Med* **27**, 2032–2040 (2021).

745 14. S. J. Zost, P. Gilchuk, R. E. Chen, J. B. Case, J. X. Reidy, A. Trivette, R. S. Nargi, R. E. Sutton, N. Suryadevara,
746 E. C. Chen, E. Binshtein, S. Shrihari, M. Ostrowski, H. Y. Chu, J. E. Didier, K. W. MacRenaris, T. Jones, S. Day, L.
747 Myers, F. Eun-Hyung Lee, D. C. Nguyen, I. Sanz, D. R. Martinez, P. W. Rothlauf, L.-M. Bloyet, S. P. J. Whelan, R.
748 S. Baric, L. B. Thackray, M. S. Diamond, R. H. Carnahan, J. E. Crowe, Rapid isolation and profiling of a diverse
749 panel of human monoclonal antibodies targeting the SARS-CoV-2 spike protein. *Nature medicine* **26**, 1422–1427
750 (2020).

751 15. N. B. Mercado, R. Zahn, F. Wegmann, C. Loos, A. Chandrashekar, J. Yu, J. Liu, L. Peter, K. McMahan, L. H.
752 Tostanoski, X. He, D. R. Martinez, L. Rutten, R. Bos, D. van Manen, J. Vellinga, J. Custers, J. P. Langedijk, T.
753 Kwaks, M. J. G. Bakkers, D. Zuijdgheest, S. K. Rosendahl Huber, C. Atyeo, S. Fischinger, J. S. Burke, J. Feldman, B.
754 M. Hauser, T. M. Caradonna, E. A. Bondzie, G. Dagotto, M. S. Gebre, E. Hoffman, C. Jacob-Dolan, M. Kirilova, Z.
755 Li, Z. Lin, S. H. Mahrokhian, L. F. Maxfield, F. Nampanya, R. Nityanandam, J. P. Nkolola, S. Patel, J. D. Ventura,
756 K. Verrington, H. Wan, L. Pessaint, A. Van Ry, K. Blade, A. Strasbaugh, M. Cabus, R. Brown, A. Cook, S.
757 Zouantchangadou, E. Teow, H. Andersen, M. G. Lewis, Y. Cai, B. Chen, A. G. Schmidt, R. K. Reeves, R. S. Baric,
758 D. A. Lauffenburger, G. Alter, P. Stoffels, M. Mammen, J. Van Hoof, H. Schuitemaker, D. H. Barouch, Single-shot
759 Ad26 vaccine protects against SARS-CoV-2 in rhesus macaques. *Nature* **586**, 583–588 (2020).

760 16. A. Tauzin, M. Nayrac, M. Benlarbi, S. Y. Gong, R. Gasser, G. Beaudoin-Bussi eres, N. Brassard, A. Laumaea, D.
761 V ezina, J. Pr evost, S. P. Anand, C. Bourassa, G. Gendron-Lepage, H. Medjahed, G. Goyette, J. Niessl, O. Tastet, L.
762 Gokool, C. Morrisseau, P. Arlotto, L. Stamatatos, A. T. McGuire, C. Larochelle, P. Uchil, M. Lu, W. Mothes, G. De
763 Serres, S. Moreira, M. Roger, J. Richard, V. Martel-Laferr iere, R. Duerr, C. Tremblay, D. E. Kaufmann, A. Finzi, A
764 single dose of the SARS-CoV-2 vaccine BNT162b2 elicits Fc-mediated antibody effector functions and T cell
765 responses. *Cell Host & Microbe* **29**, 1137–1150.e6 (2021).

766 17. K. McMahan, J. Yu, N. B. Mercado, C. Loos, L. H. Tostanoski, A. Chandrashekar, J. Liu, L. Peter, C. Atyeo, A.
767 Zhu, E. A. Bondzie, G. Dagotto, M. S. Gebre, C. Jacob-Dolan, Z. Li, F. Nampanya, S. Patel, L. Pessaint, A. Van Ry,
768 K. Blade, J. Yalley-Ogunro, M. Cabus, R. Brown, A. Cook, E. Teow, H. Andersen, M. G. Lewis, D. A.
769 Lauffenburger, G. Alter, D. H. Barouch, Correlates of protection against SARS-CoV-2 in rhesus macaques. *Nature*
770 **590**, 630–634 (2021).

771 18. S. A. Plotkin, Complex Correlates of Protection After Vaccination. *Clinical Infectious Diseases* **56**, 1458–1465
772 (2013).

773 19. S. A. Plotkin, Updates on immunologic correlates of vaccine-induced protection. *Vaccine* **38**, 2250–2257 (2020).

774 20. S. B. Bradfute, S. Bavari, Correlates of immunity to filovirus infection. *Viruses* **3**, 982–1000 (2011).

775 21. G. Dagotto, J. Yu, D. H. Barouch, Approaches and Challenges in SARS-CoV-2 Vaccine Development. *Cell Host*
776 *& Microbe* **28**, 364–370 (2020).

777 22. C. Mu oz-Fontela, W. E. Dowling, S. G. P. Funnell, P.-S. Gsell, A. X. Riveros-Balta, R. A. Albrecht, H.
778 Andersen, R. S. Baric, M. W. Carroll, M. Cavaleri, C. Qin, I. Crozier, K. Dallmeier, L. de Waal, E. de Wit, L.
779 Delang, E. Dohm, W. P. Duprex, D. Falzarano, C. L. Finch, M. B. Frieman, B. S. Graham, L. E. Gralinski, K.
780 Guilfoyle, B. L. Haagmans, G. A. Hamilton, A. L. Hartman, S. Herfst, S. J. F. Kaptein, W. B. Klimstra, I. Knezevic,
781 P. R. Krause, J. H. Kuhn, R. Le Grand, M. G. Lewis, W.-C. Liu, P. Maisonnasse, A. K. McElroy, V. Munster, N.
782 Oreshkova, A. L. Rasmussen, J. Rocha-Pereira, B. Rockx, E. Rodr guez, T. F. Rogers, F. J. Salguero, M. Schotsaert,
783 K. J. Stittelaar, H. J. Thibaut, C.-T. Tseng, J. Vergara-Alert, M. Beer, T. Brasel, J. F. W. Chan, A. Garc a-Sastre, J.
784 Neyts, S. Perlman, D. S. Reed, J. A. Richt, C. J. Roy, J. Segal s, S. S. Vasani, A. M. Henao-Restrepo, D. H. Barouch,
785 Animal models for COVID-19. *Nature* **586**, 509–515 (2020).

786 23. N. Eyal, M. Lipsitch, How to test SARS-CoV-2 vaccines ethically even after one is available. *Clin Infect Dis* ,
787 ciab182 (2021).

788 24. K. S. Corbett, B. Flynn, K. E. Foulds, J. R. Francica, S. Boyoglu-Barnum, A. P. Werner, B. Flach, S. O’Connell,
789 K. W. Bock, M. Minai, B. M. Nagata, H. Andersen, D. R. Martinez, A. T. Noe, N. Douek, M. M. Donaldson, N. N.
790 Nji, G. S. Alvarado, D. K. Edwards, D. R. Flebbe, E. Lamb, N. A. Doria-Rose, B. C. Lin, M. K. Louder, S. O’Dell,
791 S. D. Schmidt, E. Phung, L. A. Chang, C. Yap, J.-P. M. Todd, L. Pessaint, A. Van Ry, S. Browne, J. Greenhouse, T.
792 Putman-Taylor, A. Strasbaugh, T.-A. Campbell, A. Cook, A. Dodson, K. Steingrebe, W. Shi, Y. Zhang, O. M.
793 Abiona, L. Wang, A. Pegu, E. S. Yang, K. Leung, T. Zhou, I.-T. Teng, A. Widge, I. Gordon, L. Novik, R. A.
794 Gillespie, R. J. Loomis, J. I. Moliva, G. Stewart-Jones, S. Himansu, W.-P. Kong, M. C. Nason, K. M. Morabito, T. J.
795 Ruckwardt, J. E. Ledgerwood, M. R. Gaudinski, P. D. Kwong, J. R. Mascola, A. Carfi, M. G. Lewis, R. S. Baric, A.
796 McDermott, I. N. Moore, N. J. Sullivan, M. Roederer, R. A. Seder, B. S. Graham, Evaluation of the mRNA-1273
797 Vaccine against SARS-CoV-2 in Nonhuman Primates. *The New England journal of medicine* **383**, 1544–1555
798 (2020).

799 25. S. A. Plotkin, P. B. Gilbert, Nomenclature for Immune Correlates of Protection After Vaccination. *Clinical*
800 *Infectious Diseases* **54**, 1615–1617 (2012).

801 26. A. Gonçalves, J. Bertrand, R. Ke, E. Comets, X. de Lamballerie, D. Malvy, A. Pizzorno, O. Terrier, M. Rosa
802 Calatrava, F. Mentré, P. Smith, A. S. Perelson, J. Guedj, Timing of Antiviral Treatment Initiation is Critical to
803 Reduce SARS-CoV-2 Viral Load. *CPT: Pharmacometrics & Systems Pharmacology* **9**, 509–514 (2020).

804 27. K. S. Kim, K. Ejima, S. Iwanami, Y. Fujita, H. Ohashi, Y. Koizumi, Y. Asai, S. Nakaoka, K. Watashi, K. Aihara,
805 R. N. Thompson, R. Ke, A. S. Perelson, S. Iwami, A quantitative model used to compare within-host SARS-CoV-2,
806 MERS-CoV, and SARS-CoV dynamics provides insights into the pathogenesis and treatment of SARS-CoV-2. *PLoS*
807 *biology* **19**, e3001128 (2021).

808 28. A. Gonçalves, P. Maisonnasse, F. Donati, M. Albert, S. Behillil, V. Contreras, T. Naninck, R. Marlin, C. Solas,
809 A. Pizzorno, J. Lemaitre, N. Kahlaoui, O. Terrier, R. Ho Tsong Fang, V. Enouf, N. Dereuddre-Bosquet, A.
810 Brisebarre, F. Touret, C. Chapon, B. Hoen, B. Lina, M. Rosa Calatrava, X. de Lamballerie, F. Mentré, R. Le Grand,
811 S. van der Werf, J. Guedj, SARS-CoV-2 viral dynamics in non-human primates. *PLoS computational biology* **17**,
812 e1008785 (2021).

813 29. S. Wang, Y. Pan, Q. Wang, H. Miao, A. N. Brown, L. Rong, Modeling the viral dynamics of SARS-CoV-2
814 infection. *Mathematical biosciences* **328**, 108438 (2020).

815 30. A. Marc, M. Keriou, F. Blanquart, J. Bertrand, O. Mitjà, M. Corbacho-Monné, M. Marks, J. Guedj, S. E. Cobey,
816 J. W. Van der Meer, Eds. Quantifying the relationship between SARS-CoV-2 viral load and infectiousness. *eLife* **10**,
817 e69302 (2021).

818 31. R. Ke, C. Zitzmann, D. D. Ho, R. M. Ribeiro, A. S. Perelson, In vivo kinetics of SARS-CoV-2 infection and its
819 relationship with a person’s infectiousness. *Proceedings of the National Academy of Sciences* **118**, e2111477118
820 (2021).

821 32. M. A. Myers, A. P. Smith, L. C. Lane, D. J. Moquin, R. Aogo, S. Woolard, P. Thomas, P. Vogel, A. M. Smith, J.
822 T. Schiffer, S. L. Sawyer, J. T. Schiffer, Eds. Dynamically linking influenza virus infection kinetics, lung injury,
823 inflammation, and disease severity. *eLife* **10**, e68864 (2021).

824 33. P. Baccam, C. Beauchemin, C. A. Macken, F. G. Hayden, A. S. Perelson, Kinetics of Influenza A Virus Infection
825 in Humans. *Journal of Virology* **80**, 7590–7599 (2006).

826 34. A. Goyal, L. E. Liao, A. S. Perelson, Within-host mathematical models of hepatitis B virus infection: Past,
827 present, and future. *Current Opinion in Systems Biology* **18**, 27–35 (2019).

828 35. A. Goyal, R. M. Ribeiro, A. S. Perelson, The Role of Infected Cell Proliferation in the Clearance of Acute HBV
829 Infection in Humans. *Viruses* **9**, 350 (2017).

36. R. Marlin, V. Godot, S. Cardinaud, M. Galhaut, S. Coleon, S. Zurawski, N. Dereuddre-Bosquet, M. Cavarelli, A.-S. Gallouët, P. Maisonnasse, L. Dupaty, C. Fenwick, T. Naninck, J. Lemaitre, M. Gomez-Pacheco, N. Kahlaoui, V. Contreras, F. Relouzat, R. H. T. Fang, Z. Wang, J. Ellis, C. Chapon, M. Centlivre, A. Wiedemann, C. Lacabartz, M. Surenaud, I. Szurgot, P. Liljeström, D. Planas, T. Bruel, O. Schwartz, S. van der Werf, G. Pantaleo, M. Prague, R. Thiébaud, G. Zurawski, Y. Lévy, R. L. Grand, Targeting SARS-CoV-2 receptor-binding domain to cells expressing CD40 improves protection to infection in convalescent macaques. *Nat Commun* **12**, 5215 (2021).

37. A.-L. Flamar, S. Zurawski, F. Scholz, I. Gayet, L. Ni, X.-H. Li, E. Klechevsky, J. Quinn, S. Oh, D. H. Kaplan, J. Banchereau, G. Zurawski, Noncovalent assembly of anti-dendritic cell antibodies and antigens for evoking immune responses in vitro and in vivo. *Journal of immunology (Baltimore, Md. : 1950)* **189**, 2645–55 (2012).

38. G. Zurawski, X. Shen, S. Zurawski, G. D. Tomaras, D. C. Montefiori, M. Roederer, G. Ferrari, C. Lacabartz, P. Klucar, Z. Wang, K. E. Foulds, S.-F. Kao, X. Yu, A. Sato, N. L. Yates, C. LaBranche, S. Stanfield-Oakley, K. Kibler, B. Jacobs, A. Salazar, S. Self, W. Fulp, R. Gottardo, L. Galmin, D. Weiss, A. Cristillo, G. Pantaleo, Y. Levy, Superiority in Rhesus Macaques of Targeting HIV-1 Env gp140 to CD40 versus LOX-1 in Combination with Replication-Competent NYVAC-KC for Induction of Env-Specific Antibody and T Cell Responses. *Journal of Virology* **91**, e01596-16.

39. L. Cheng, Q. Wang, G. Li, R. Banga, J. Ma, H. Yu, F. Yasui, Z. Zhang, G. Pantaleo, M. Perreau, S. Zurawski, G. Zurawski, Y. Levy, L. Su, TLR3 agonist and CD40-targeting vaccination induces immune responses and reduces HIV-1 reservoirs. *The Journal of clinical investigation* **128**, 4387–4396 (2018).

40. V. Godot, C. Tcherakian, L. Gil, I. Cervera-Marzal, G. Li, L. Cheng, N. Ortonne, J.-D. Lelièvre, G. Pantaleo, C. Fenwick, M. Centlivre, H. Mouquet, S. Cardinaud, S. M. Zurawski, G. Zurawski, P. Milpied, L. Su, Y. Lévy, TLR-9 agonist and CD40-targeting vaccination induces HIV-1 envelope-specific B cells with a diversified immunoglobulin repertoire in humanized mice. *PLoS pathogens* **16**, e1009025 (2020).

41. P. Baccam, C. Beauchemin, C. A. Macken, F. G. Hayden, A. S. Perelson, Kinetics of Influenza A Virus Infection in Humans. *Journal of Virology* **80**, 7590–7599 (2006).

42. R. Ke, C. Zitzmann, R. M. Ribeiro, A. S. Perelson, *Kinetics of SARS-CoV-2 infection in the human upper and lower respiratory tracts and their relationship with infectiousness* (medRxiv, 2020; <https://www.medrxiv.org/content/10.1101/2020.09.25.20201772v1>).

43. L. Pinky, C. W. Burke, C. J. Russell, A. M. Smith, Quantifying dose-, strain-, and tissue-specific kinetics of parainfluenza virus infection. *PLOS Computational Biology* **17**, e1009299 (2021).

44. R. Robinot, M. Hubert, G. D. de Melo, F. Lazarini, T. Bruel, N. Smith, S. Levallois, F. Larrous, J. Fernandes, S. Gellenoncourt, S. Rigaud, O. Gorgette, C. Thouvenot, C. Trébeau, A. Mallet, G. Duménil, S. Gobaa, R. Etournay, P.-M. Lledo, M. Lecuit, H. Bourhy, D. Duffy, V. Michel, O. Schwartz, L. A. Chakrabarti, SARS-CoV-2 infection induces the dedifferentiation of multiciliated cells and impairs mucociliary clearance. *Nat Commun* **12**, 4354 (2021).

45. P. J. M. Brouwer, M. Brinkkemper, P. Maisonnasse, N. Dereuddre-Bosquet, M. Grobbsen, M. Claireaux, M. de Gast, R. Marlin, V. Chesnais, S. Dity, J. D. Allen, Y. Watanabe, J. M. Giezen, G. Kerster, H. L. Turner, K. van der Straten, C. A. van der Linden, Y. Aldon, T. Naninck, I. Bontjer, J. A. Burger, M. Poniman, A. Z. Mykytyn, N. M. A. Okba, E. E. Schermer, M. J. van Breemen, R. Ravichandran, T. G. Caniels, J. van Schooten, N. Kahlaoui, V. Contreras, J. Lemaitre, C. Chapon, R. H. T. Fang, J. Villaudy, K. Sliepen, Y. U. van der Velden, B. L. Haagmans, G. J. de Bree, E. Ginoux, A. B. Ward, M. Crispin, N. P. King, S. van der Werf, M. J. van Gils, R. Le Grand, R. W. Sanders, Two-component spike nanoparticle vaccine protects macaques from SARS-CoV-2 infection. *Cell* **184**, 1188-1200.e19 (2021).

46. A. W. Chung, M. P. Kumar, K. B. Arnold, W. H. Yu, M. K. Schoen, L. J. Dunphy, T. J. Suscovich, N. Frahm, C. Linde, A. E. Mahan, M. Hoffner, H. Streeck, M. E. Ackerman, M. J. McElrath, H. Schuitemaker, M. G. Pau, L. R. Baden, J. H. Kim, N. L. Michael, D. H. Barouch, D. A. Lauffenburger, G. Alter, Dissecting Polyclonal Vaccine-Induced Humoral Immunity against HIV Using Systems Serology. *Cell* **163**, 988–98 (2015).

875 47. J. Dufloo, L. Grzelak, I. Staropoli, Y. Madec, L. Tondeur, F. Anna, S. Pelleau, A. Wiedemann, C. Planchais, J.
876 Buchrieser, R. Robinot, M.-N. Ungeheuer, H. Mouquet, P. Charneau, M. White, Y. Lévy, B. Hoen, A. Fontanet, O.
877 Schwartz, T. Bruel, Asymptomatic and symptomatic SARS-CoV-2 infections elicit polyfunctional antibodies. *Cell*
878 *reports. Medicine* **2**, 100275 (2021).

879 48. G. Alter, J. Yu, J. Liu, A. Chandrashekar, E. N. Borducchi, L. H. Tostanoski, K. McMahan, C. Jacob-Dolan, D.
880 R. Martinez, A. Chang, T. Anioke, M. Lifton, J. Nkolola, K. E. Stephenson, C. Atyeo, S. Shin, P. Fields, I. Kaplan,
881 H. Robins, F. Amanat, F. Krammer, R. S. Baric, M. Le Gars, J. Sadoff, A. M. de Groot, D. Heerwegh, F. Struyf, M.
882 Douoguih, J. van Hoof, H. Schuitemaker, D. H. Barouch, Immunogenicity of Ad26.COV2.S vaccine against SARS-
883 CoV-2 variants in humans. *Nature* **596**, 268–272 (2021).

884 49. P. Jin, J. Li, H. Pan, Y. Wu, F. Zhu, Immunological surrogate endpoints of COVID-2019 vaccines: the evidence
885 we have versus the evidence we need. *Signal transduction and targeted therapy* **6**, 48 (2021).

886 50. K. R. W. Emary, T. Golubchik, P. K. Aley, C. V Ariani, B. Angus, S. Bibi, B. Blane, D. Bonsall, P. Cicconi, S.
887 Charlton, E. A. Clutterbuck, A. M. Collins, T. Cox, T. C. Darton, C. Dold, A. D. Douglas, C. J. A. Duncan, K. J.
888 Ewer, A. L. Flaxman, S. N. Faust, D. M. Ferreira, S. Feng, A. Finn, P. M. Folegatti, M. Fuskova, E. Galiza, A. L.
889 Goodman, C. M. Green, C. A. Green, M. Greenland, B. Hallis, P. T. Heath, J. Hay, H. C. Hill, D. Jenkin, S.
890 Kerridge, R. Lazarus, V. Libri, P. J. Lillie, C. Ludden, N. G. Marchevsky, A. M. Minassian, A. C. McGregor, Y. F.
891 Mujadidi, D. J. Phillips, E. Pleded, K. M. Pollock, H. Robinson, A. Smith, R. Song, M. D. Snape, R. K. Sutherland,
892 E. C. Thomson, M. Toshner, D. P. J. Turner, J. Vekemans, T. L. Villafana, C. J. Williams, A. V. S. Hill, T. Lambe,
893 S. C. Gilbert, M. Voysey, M. N. Ramasamy, A. J. Pollard, COVID-19 Genomics UK consortium, AMPHEUS
894 Project, Oxford COVID-19 Vaccine Trial Group, Efficacy of ChAdOx1 nCoV-19 (AZD1222) vaccine against
895 SARS-CoV-2 variant of concern 202012/01 (B.1.1.7): an exploratory analysis of a randomised controlled trial.
896 *Lancet (London, England)* **397**, 1351–1362 (2021).

897 51. A. Chandrashekar, J. Liu, A. J. Martinot, K. McMahan, N. B. Mercado, L. Peter, L. H. Tostanoski, J. Yu, Z.
898 Maliga, M. Nekorchuk, K. Busman-Sahay, M. Terry, L. M. Wrijil, S. Ducat, D. R. Martinez, C. Atyeo, S.
899 Fischinger, J. S. Burke, M. D. Slein, L. Pessaint, A. Van Ry, J. Greenhouse, T. Taylor, K. Blade, A. Cook, B.
900 Finneyfrock, R. Brown, E. Teow, J. Velasco, R. Zahn, F. Wegmann, P. Abbink, E. A. Bondzie, G. Dagotto, M. S.
901 Gebre, X. He, C. Jacob-Dolan, N. Kordana, Z. Li, M. A. Lifton, S. H. Mahrokhian, L. F. Maxfield, R. Nityanandam,
902 J. P. Nkolola, A. G. Schmidt, A. D. Miller, R. S. Baric, G. Alter, P. K. Sorger, J. D. Estes, H. Andersen, M. G.
903 Lewis, D. H. Barouch, SARS-CoV-2 infection protects against rechallenge in rhesus macaques. *Science (New York,*
904 *N.Y.)* **369**, 812–817 (2020).

905 52. N. H. L. Leung, D. K. W. Chu, E. Y. C. Shiu, K.-H. Chan, J. J. McDevitt, B. J. P. Hau, H.-L. Yen, Y. Li, D. K.
906 M. Ip, J. S. M. Peiris, W.-H. Seto, G. M. Leung, D. K. Milton, B. J. Cowling, Respiratory virus shedding in exhaled
907 breath and efficacy of face masks. *Nat Med* **26**, 676–680 (2020).

908 53. M. Marks, P. Millat-Martinez, D. Ouchi, C. h Roberts, A. Alemany, M. Corbacho-Monné, M. Ubals, A. Tobias,
909 C. Tebé, E. Ballana, Q. Bassat, B. Baro, M. Vall-Mayans, C. G-Beiras, N. Prat, J. Ara, B. Clotet, O. Mitjà,
910 Transmission of COVID-19 in 282 clusters in Catalonia, Spain: a cohort study. *The Lancet Infectious Diseases* **21**,
911 629–636 (2021).

912 54. N. Néant, G. Lingas, Q. L. Hingrat, J. Ghosn, I. Engelmann, Q. Lepiller, A. Gaymard, V. Ferré, C. Hartard, J.-C.
913 Plantier, V. Thibault, J. Marlet, B. Montes, K. Bouiller, F.-X. Lescure, J.-F. Timsit, E. Faure, J. Poissy, C. Chidiac,
914 F. Raffi, A. Kimmoun, M. Etienne, J.-C. Richard, P. Tattevin, D. Garot, V. L. Moing, D. Bachelet, C. Tardivon, X.
915 Duval, Y. Yazdanpanah, F. Mentré, C. Laouénan, B. Visseaux, J. Guedj, for the F. C. C. I. and F. C. S. Groups,
916 Modeling SARS-CoV-2 viral kinetics and association with mortality in hospitalized patients from the French
917 COVID cohort. *PNAS* **118** (2021), doi:10.1073/pnas.2017962118.

918 55. C. Gutmann, K. Takov, S. A. Burnap, B. Singh, H. Ali, K. Theofilatos, E. Reed, M. Hasman, A. Nabeebaccus,
919 M. Fish, M. J. McPhail, K. O’Gallagher, L. E. Schmidt, C. Cassel, M. Rienks, X. Yin, G. Auzinger, S. Napoli, S. F.
920 Mujib, F. Trovato, B. Sanderson, B. Merrick, U. Niazi, M. Saqi, K. Dimitrakopoulou, R. Fernández-Leiro, S. Braun,
921 R. Kronstein-Wiedemann, K. J. Doores, J. D. Edgeworth, A. M. Shah, S. R. Bornstein, T. Tonn, A. C. Hayday, M.

922 Giacca, M. Shankar-Hari, M. Mayr, SARS-CoV-2 RNAemia and proteomic trajectories inform prognostication in
923 COVID-19 patients admitted to intensive care. *Nat Commun* **12**, 3406 (2021).

924 56. T. Charmet, L. Schaeffer, R. Grant, S. Galmiche, O. Chény, C. Von Platen, A. Maurizot, A. Rogoff, F. Omar, C.
925 David, A. Septfons, S. Cauchemez, A. Gaymard, B. Lina, L. H. Lefrancois, V. Enouf, S. van der Werf, A. Mailles,
926 D. Levy-Bruhl, F. Carrat, A. Fontanet, Impact of original, B.1.1.7, and B.1.351/P.1 SARS-CoV-2 lineages on
927 vaccine effectiveness of two doses of COVID-19 mRNA vaccines: Results from a nationwide case-control study in
928 France. *The Lancet Regional Health - Europe* **8**, 100171 (2021).

929 57. T. Nyberg, N. M. Ferguson, S. G. Nash, H. H. Webster, S. Flaxman, N. Andrews, W. Hinsley, J. L. Bernal, M.
930 Kall, S. Bhatt, P. Blomquist, A. Zaidi, E. Volz, N. A. Aziz, K. Harman, S. Funk, S. Abbott, T. Nyberg, N. M.
931 Ferguson, S. G. Nash, H. H. Webster, S. Flaxman, N. Andrews, W. Hinsley, J. Lopez Bernal, M. Kall, S. Bhatt, P.
932 Blomquist, A. Zaidi, E. Volz, N. Abdul Aziz, K. Harman, S. Funk, S. Abbott, R. Hope, A. Charlett, M. Chand, A. C.
933 Ghani, S. R. Seaman, G. Dabrera, D. De Angelis, A. M. Presanis, S. Thelwall, R. Hope, A. Charlett, M. Chand, A. C.
934 Ghani, S. R. Seaman, G. Dabrera, D. De Angelis, A. M. Presanis, S. Thelwall, Comparative analysis of the risks of
935 hospitalisation and death associated with SARS-CoV-2 omicron (B.1.1.529) and delta (B.1.617.2) variants in
936 England: a cohort study. *The Lancet* **399**, 1303–1312 (2022).

937 58. K. E. Kester, J. F. Cummings, O. Ofori-Anyinam, C. F. Ockenhouse, U. Krzych, P. Moris, R. Schwenk, R. A.
938 Nielsen, Z. Debebe, E. Pinelis, L. Juompan, J. Williams, M. Dowler, V. A. Stewart, R. A. Wirtz, M.-C. Dubois, M.
939 Lievens, J. Cohen, W. R. Ballou, D. G. Heppner, RTS,S Vaccine Evaluation Group, Randomized, double-blind,
940 phase 2a trial of falciparum malaria vaccines RTS,S/AS01B and RTS,S/AS02A in malaria-naïve adults: safety,
941 efficacy, and immunologic associates of protection. *The Journal of infectious diseases* **200**, 337–46 (2009).

942 59. K. J. Travaglini, A. N. Nabhan, L. Penland, R. Sinha, A. Gillich, R. V Sit, S. Chang, S. D. Conley, Y. Mori, J.
943 Seita, G. J. Berry, J. B. Shrager, R. J. Metzger, C. S. Kuo, N. Neff, I. L. Weissman, S. R. Quake, M. A. Krasnow, A
944 molecular cell atlas of the human lung from single-cell RNA sequencing. *Nature* **587**, 619–625 (2020).

945 60. A. Pizzorno, B. Padey, T. Julien, S. Trouillet-Assant, A. Traversier, E. Errazuriz-Cerda, J. Fouret, J. Dubois, A.
946 Gaymard, F.-X. Lescure, V. Dulière, P. Brun, S. Constant, J. Poissy, B. Lina, Y. Yazdanpanah, O. Terrier, M. Rosa-
947 Calatrava, Characterization and Treatment of SARS-CoV-2 in Nasal and Bronchial Human Airway Epithelia. *Cell*
948 *Reports Medicine* **1**, 100059 (2020).

949 61. A. Gonçalves, P. Maisonnasse, F. Donati, M. Albert, S. Behillil, V. Contreras, T. Naninck, R. Marlin, C. Solas,
950 A. Pizzorno, J. Lemaitre, N. Kahlaoui, O. Terrier, R. H. T. Fang, V. Enouf, N. Dereuddre-Bosquet, A. Brisebarre, F.
951 Touret, C. Chapon, B. Hoen, B. Lina, M. R. Calatrava, X. de Lamballerie, F. Mentré, R. L. Grand, S. van der Werf,
952 J. Guedj, SARS-CoV-2 viral dynamics in non-human primates. *PLOS Computational Biology* **17**, e1008785 (2021).

953 62. A. P. Smith, D. J. Moquin, V. Bernhauerova, A. M. Smith, Influenza Virus Infection Model With Density
954 Dependence Supports Biphasic Viral Decay. *Frontiers in Microbiology* **9** (2018).

955 63. U. G. Dafni, A. A. Tsiatis, Evaluating surrogate markers of clinical outcome when measured with error.
956 *Biometrics* **54**, 1445–1462 (1998).

957 64. R. J. Carroll, D. Ruppert, L. A. Stefanski, C. M. Crainiceanu, *Measurement Error in Nonlinear Models: A*
958 *Modern Perspective, Second Edition* (Chapman and Hall/CRC, New York, ed. 2, 2006).

959 65. L. Wu, *Mixed Effects Models for Complex Data* (Chapman and Hall/CRC, New York, 2009).

960 66. G. Lui, L. Ling, C. K. Lai, E. Y. Tso, K. S. Fung, V. Chan, T. H. Ho, F. Luk, Z. Chen, J. K. Ng, K. Chow, P. K.
961 Cheng, R. C. Chan, D. N. Tsang, C. D. Gomersall, D. S. Hui, P. K. Chan, Viral dynamics of SARS-CoV-2 across a
962 spectrum of disease severity in COVID-19. *Journal of Infection* **81**, 318–356 (2020).

963 67. A. Goyal, E. R. Duke, E. F. Cardozo-Ojeda, J. T. Schiffer, Mathematical modeling explains differential SARS
964 CoV-2 kinetics in lung and nasal passages in remdesivir treated rhesus macaques. *Biorxiv* , 2020.06.21.163550
965 (2020).

68. I. Balelli, C. Pasin, M. Prague, F. Crauste, T. V. Effelterre, V. Bockstal, L. Solfrosi, R. Thiébaud, A model for establishment, maintenance and reactivation of the immune response after vaccination against Ebola virus. *Journal of Theoretical Biology* **495**, 110254 (2020).

69. A. J. Pollard, E. M. Bijker, A guide to vaccinology: from basic principles to new developments. *Nature reviews. Immunology* **21**, 83–100 (2021).

70. S. J. Rhodes, J. Guedj, H. A. Fletcher, T. Lindenstrøm, T. J. Scriba, T. G. Evans, G. M. Knight, R. G. White, Using vaccine Immunostimulation/Immunodynamic modelling methods to inform vaccine dose decision-making. *NPJ vaccines* **3**, 36 (2018).

71. C. Gaebler, Z. Wang, J. C. C. Lorenzi, F. Muecksch, S. Finkin, M. Tokuyama, A. Cho, M. Jankovic, D. Schaefer-Babajew, T. Y. Oliveira, M. Cipolla, C. Viant, C. O. Barnes, Y. Bram, G. Breton, T. Hägglöf, P. Mendoza, A. Hurley, M. Turroja, K. Gordon, K. G. Millard, V. Ramos, F. Schmidt, Y. Weisblum, D. Jha, M. Tankelevich, G. Martinez-Delgado, J. Yee, R. Patel, J. Dizon, C. Unson-O'Brien, I. Shimeliovich, D. F. Robbiani, Z. Zhao, A. Gazumyan, R. E. Schwartz, T. Hatzioannou, P. J. Bjorkman, S. Mehndru, P. D. Bieniasz, M. Caskey, M. C. Nussenzweig, Evolution of antibody immunity to SARS-CoV-2. *Nature* **591**, 639–644 (2021).

72. K. Vanshylla, V. Di Cristanziano, F. Kleipass, F. Dewald, P. Schommers, L. Gieselmann, H. Gruell, M. Schlotz, M. S. Ercanoglu, R. Stumpf, P. Mayer, M. Zehner, E. Heger, W. Johannis, C. Horn, I. Suárez, N. Jung, S. Salomon, K. A. Eberhardt, B. Gathof, G. Fätkenheuer, N. Pfeifer, R. Eggeling, M. Augustin, C. Lehmann, F. Klein, Kinetics and correlates of the neutralizing antibody response to SARS-CoV-2 infection in humans. *Cell host & microbe* **29**, 917-929.e4 (2021).

73. A. Goyal, D. B. Reeves, J. T. Schiffer, Multi-scale modelling reveals that early super-spreader events are a likely contributor to novel variant predominance. *Journal of The Royal Society Interface* **19**, 20210811.

74. C. Fenwick, A. Croxatto, A. T. Coste, F. Pojer, C. André, C. Pellaton, A. Farina, J. Campos, D. Hacker, K. Lau, B.-J. Bosch, S. Gonseth Nussle, M. Bochud, V. D'Acremont, D. Trono, G. Greub, G. Pantaleo, Changes in SARS-CoV-2 Spike versus Nucleoprotein Antibody Responses Impact the Estimates of Infections in Population-Based Seroprevalence Studies. *Journal of Virology* **95**, e01828-20.

75. M. Johnson, H. R. Wagstaffe, K. C. Gilmour, A. L. Mai, J. Lewis, A. Hunt, J. Sirr, C. Bengt, L. Grandjean, D. Goldblatt, Evaluation of a novel multiplexed assay for determining IgG levels and functional activity to SARS-CoV-2. *Journal of clinical virology: the official publication of the Pan American Society for Clinical Virology* **130**, 104572 (2020).

76. S. G. Sawicki, D. L. Sawicki, S. G. Siddell, A Contemporary View of Coronavirus Transcription. *Journal of Virology* **81**, 20–29 (2007).

77. H. Miao, X. Xia, A. S. Perelson, H. Wu, On Identifiability of Nonlinear ODE Models and Applications in Viral Dynamics. *SIAM Review* **53**, 3–39 (2011).

78. B. Asgharian, O. Price, G. McClellan, R. Corley, D. R. Einstein, R. E. Jacob, J. Harkema, S. A. Carey, E. Schelegle, D. Hyde, J. S. Kimbell, F. J. Miller, Development of a rhesus monkey lung geometry model and application to particle deposition in comparison to humans. *Inhalation toxicology* **24**, 869–99 (2012).

79. H.-T. Thai, F. Mentré, N. H. G. Holford, C. Veyrat-Follet, E. Comets, Evaluation of bootstrap methods for estimating uncertainty of parameters in nonlinear mixed-effects models: a simulation study in population pharmacokinetics. *Journal of Pharmacokinetics and Pharmacodynamics* **41**, 15–33 (2014).

80. M. Z. I. Chowdhury, T. C. Turin, Variable selection strategies and its importance in clinical prediction modelling. *Fam Med Community Health* **8**, e000262 (2020).

Acknowledgments: We would like to thank J. Guedj and O. Terrier for fruitful discussions on the model definition. We thank S. Langlois, J. Demilly, N. Dhooge, P. Le Calvez, M. Potier, J. M. Robert, T. Prot, and C. Dodan for the NHP experiments; L. Bossevot, M. Leonec, L. Moenne-Loccoz, M. Calpin-Lebreau, and J. Morin for the RT-qPCR, ELISpot and Luminex assays, and for the preparation of reagents; A-S. Gallouët, M. Gomez-Pacheco and W. Gros for NHP T-cell assays and flow cytometry; B. Fert for her help with the CT scans; M. Barendji, J. Dinh and E. Guyon for the NHP sample processing; S. Keyser for the transports organization; F. Ducancel and Y. Gorin for their help with the logistics and safety management; I. Mangeot for here help with resources management and B. Targat contributed to data management. The monkey and syringe pictures in Fig.1 was created with BioRender.com. This work was supported by INSERM and the Investissements d’Avenir program, Vaccine Research Institute (VRI), managed by the ANR under reference ANR-10-LABX-77-01. MA has been funded by INRIA PhD grant. The Infectious Disease Models and Innovative Therapies (IDMIT) research infrastructure is supported by the “Programme Investissements d’Avenir”, managed by the ANR under reference ANR-11-INBS-0008. The Fondation Bettencourt Schueller and the Region Ile-de-France contributed to the implementation of IDMIT’s facilities and imaging technologies used to define volume of respiratory tract. The NHP study received financial support from REACTing, the Fondation pour la Recherche Medicale (FRM; AM-CoV-Path). We thank Lixoft SAS for their support. Numerical computations were in part carried out using the PlaFRIM experimental testbed, supported by Inria, CNRS (LABRI and IMB), Université de Bordeaux, Bordeaux INP and Conseil Régional d’Aquitaine (see <https://www.plafrim.fr>). We thank Miles Davenport and Frederik Graw as Senior Editor and Reviewing Editor of our paper, respectively, and the three anonymous reviewers for their time and their constructive comments.

Competing interests: Authors declare that they have no competing interests

Data and materials availability: No unique reagents were generated for this study.

Data that support the findings of this study are provided in the source data files of this paper and gather data from 1) the study (36) used in this analysis, which are also directly available online in the section **Source data** of this related paper (<https://www.nature.com/articles/s41467-021-25382-0#Sec17>) ; 2) the study (45) used in this analysis, which are also available from the corresponding authors of the related paper and 3) the study (24) used in this analysis, which are also available online in the section **Supplementary Material** of the related paper, excel file labelled (“Supplementary Appendix 2”). Data from the main study (36) can also be found in the open-access repository Dryad using the following DOI: <https://doi.org/10.5061/dryad.1zcrjdfv7>. The original code (mlxtran models and R) as well as model definition files including the full list of parameters used are available and free-of-cost on github (Inria SISTM Team) at the following link: <https://github.com/sistm/SARSCoV2modelingNHP>.

Figures

Figure 1. Design of the study 1 and viral dynamics.

(A) *Study design.* Cynomolgus macaques (*Macaca fascicularis*), aged 37-58 months (8 females and 13 males). 24-26 weeks post infection with SARS-CoV-2, twelve of these animals were randomly assigned in two experimental groups. The convalescent vaccinated group (n=6) received 200 µg of αCD40.RBD vaccine. The other six convalescent animals were used as controls. Additional six age matched (43.7 months +/-6.76) cynomolgus macaques from same origin were included in the study as controls naive from any exposure to SARS-CoV-2. Four weeks after immunization, all animals were exposed to a total dose of 10^6 pfu of SARS-CoV-2 virus via the combination of intra-nasal and intra-tracheal routes. In this work, only data collected from the 2nd exposure were considered. (B) Individual log₁₀ transformed gRNA viral load dynamics in nasopharyngeal swabs (top) and tracheal swabs (bottom) after the initial exposure to SARS-CoV-2 in naive macaques (black, right) and after the second exposure in convalescent (blue, middle) and αCD40.RBD-vaccinated convalescent (green, left) groups. Horizontal red dashed lines indicate the limit of quantification.

Figure 2. Mechanistic modelling.

(A) Description of the model in the two compartments: the nasopharynx and the trachea. (B) Model fit to the log₁₀ transformed observed gRNA viral loads in tracheal (top) and nasopharyngeal (bottom) compartments after the initial exposure to SARS-CoV-2 in naive macaques (black, right) and after the second exposure in convalescent (blue, middle) and vaccinated (green, left) animals. Thick solid and dashed lines indicate mean viral load dynamics predicted and observed, respectively. Shaded areas indicate the 95% confidence intervals of the predictions. Dots represents observations. (C) Model predictions of unobserved quantities in the tracheal compartment for naive (black, solid lines), convalescent (blue, dashed lines) and vaccinated (green, dotted lines) animals: target cells as percentage of the value at the challenge (top, left), infected cells (top, middle), productively infected cells (top, right), inoculum (bottom, right), infectious (bottom, left) and non-infectious virus (bottom, middle). Thick lines indicate mean values over time within each group. Shaded areas indicate the 95% confidence interval. Horizontal dashed red lines indicate the limit of quantification and horizontal solid red lines highlight the threshold of one infected cell.

Figure 3. Harvest times and measurements.

Nasopharyngeal and tracheal fluids, were collected at 0, 1, 2, 3, 4, 6, 9, 14 and 20 days post exposure (d.p.e) while blood was taken at 0, 2, 4, 6, 9, 14 and 20 d.p.e. Genomic and subgenomic viral loads were

measured by RT-qPCR. Anti-Spike IgG sera were titrated by multiplex bead assay, Anti-RBD and anti-Nucleocapside (N) IgG were titrated using a commercially available multiplexed immunoassay developed by Mesoscale Discovery (MSD, Rockville, MD). The MSD pseudo-neutralization assay was used to measure antibodies neutralizing the binding of the spike protein and RBD to the ACE2 receptor. Neutralizing antibodies against B.1.1.7, B.1.351 and D614G strains were measured by S-Fuse neutralization assay and expressed as ED50 (Effective dose 50%). T-cell responses were characterized as the frequency of PBMC expressing cytokines (IL-2, IL-17 a, IFN- γ , TNF-a, IL-13, CD137 and CD154) after stimulation with S or N sequence overlapping peptide pools. IFN- γ ELISpot assay of PBMCs were performed on PBMC stimulated with RBD or N sequence overlapping peptide pools and expressed as spot forming cell (SFC) per 1.0×10^6 PBMC.

Figure 4. Immune markers.

(A) Dynamics of biomarker selected as mCoP. Quantification of antibodies inhibiting RBD-ACE2 binding, measured by the MSD pseudo-neutralization assay (ECL, in AU) (top) and anti-RBD IgG titrated by ELISA assay (in IgG titer) (bottom). Thin lines represent individual values. Thick lines indicate medians of observations within naïve (black, solid line), convalescent (blue, dashed line) and α CD40.RBD-vaccinated convalescent (green, dotted line) animals. Shaded areas indicate 5th-95th confidence intervals of observations. **(B) Systematic screening of effect of the markers.** For every single marker, a model has been fitted to explore whether it explains the variation of the parameter of interest better or as well than the group indicator. Parameters of interest were β , the infection rate of ACE2+ target cells, and δ , the loss rate of infected cells. Models were compared according to the Bayesian Information Criterion (BIC), the lower being the better. The green line represents the reference model that includes the group effect (naive/convalescent/vaccinated) without any adjustment for immunological marker (see **Figure 3** for more details about measurement of immunological markers). **(C) Thresholds of inhibition of RBD-ACE2 binding.** Estimated infection rate (in $(\text{copies/mL})^{-1} \text{ day}^{-1}$) of target cells according to the quantification of antibodies inhibiting RBD-ACE2 (in ECL) at exposure. Thin dotted lines and circles represent individual values of infection rates (right axis) and neutralizing antibodies (left axis). Shaded areas delimit the pseudo-neutralization / viral infectivity relationships within each group. **(D) Reproduction number over time.** Model predictions of the reproduction number over time in the trachea (right) and nasopharynx (left). The reproduction number is representing the number of infected cells from one infected cell if target cells are unlimited. Below one, the effective reproduction number indicates that the infection is going to be cured. Horizontal solid red lines highlight the threshold of one. Same legend than A). **(E) Conditions for controlling the infection.** Basic reproduction number (R_0) at the time of the challenge according to the levels of antibodies inhibiting RBD-ACE2 binding (the lower the better) and of

anti-RBD IgG binding antibodies (the higher the better) assuming they are mechanistic correlates of blocking new cell infection and promoting infected cell death, respectively. The red area with $R > 1$ describes a situation where the infection is spreading. The green area with $R < 1$ describes a situation where the infection is controlled. The dotted red line delimitates the two areas. Black long dashed lines represent the values of neutralizing and binding antibodies measured at exposure. Observed values for three different animals belonging to the naive (bottom, right), convalescent (bottom, left) and vaccinated (top, left) groups are represented. For each animal, individual values of R_0 were estimated considering their individual values of the model parameters (β and δ).

Figure 5. The second study testing two-component spike nanoparticle vaccine.

(A) Study design. Cynomolgus macaques were randomly assigned in two experimental groups. Twelve, eight and two weeks post-infection with SARS-CoV-2 virus, six of them were successively immunized with 50 μ g of SARS-CoV-2 S-I53-50NP vaccine. The four other animals received no vaccination. Two weeks after the final immunization, all monkeys were exposed to a total dose of 106 pfu of SARS-CoV-2 virus via intra-nasal and intra-tracheal routes. **(B)** Harvest times and measurements. Nasopharyngeal and tracheal fluids were collected at 0, 1, 2, 3, 4, 5, 6, 10, 14 and 21 d.p.e while blood was taken at 0, 2, 4, 6, 10, 14 and 21 d.p.e. Genomic and subgenomic viral loads were measured by RT-qPCR. Anti-Spike, anti-RBD and anti-Nucleocapside (N) IgG were titrated using a multiplexed immunoassay developed by Mesoscale Discovery (MSD, Rockville, MD) and expressed in AU/mL. The MSD pseudo-neutralization assay was used to quantify antibodies neutralizing the binding of the spike protein and RBD domain to the ACE2 receptor and results were expressed in ECL. **(C)** Genomic viral load dynamics in nasopharyngeal and tracheal swabs after the exposure to SARS-Cov-2 in naive (black, solid line) and vaccinated (green, dashed line) animals. Thin lines represent individual values. Thick lines indicate medians within each group. **(D)** Model fit to the log10-transformed observed gRNA viral load in nasopharynx and trachea after the exposure to SARS-CoV-2 in naïve and vaccinated macaques. Solid thin lines indicate individual dynamics predicted by the model adjusted for groups. Thick dashed lines indicate mean viral load over time. **(E)** Thresholds of inhibition of RBD-ACE2 binding. Estimated infection rate of target cells ((copies/mL)-1day⁻¹) according to the quantification of antibodies inhibiting RBD-ACE2 binding (ECL) at exposure for naive (black) and vaccinated (green) animals. Thin dotted lines and circles represent individual infection rates (right axis) and neutralizing antibodies (left axis). Thick dashed lines and dashed areas delimit the pseudo-neutralization / viral infectivity relationships within each group. (C,D) Horizontal red dashed lines represent the limit of quantification and shaded areas the 95% confidence intervals.

Supplementary Figures

Figure 1 – figure supplement 1. Viral dynamics after the first exposure to SARS-CoV-2 and biomarker measurements from the first to the second exposure to SARS-CoV-2.

(A) Individual \log_{10} transformed gRNA viral load dynamics in nasopharyngeal (left) and tracheal (right) swabs after the initial exposure to SARS-CoV-2 in naive macaques (n=12). Solid lines represent individual values. Horizontal red dashed lines indicate the limit of quantification. (B) Relative MFI of IgG binding to SARS-CoV-2 Spike protein, measured using a Luminex-based serology assay, in serum samples, after the initial exposure to SARS-CoV-2. (C) Quantification of antibodies inhibiting the attachment of Spike protein to ACE2 receptor in NHP serum, measured by the Mesoscale Discovery (MSD, Rockville, MD) pseudo-neutralization assay. Results are expressed as ECL (ECL, Electro-chemiluminescence) in AU. (D) Quantification of SARS-CoV-2 IgG binding N or RBD domain measured in the serum of NHPs titrated by ELISA assay. Results are expressed in IgG titer. (E) Quantification of SARS-CoV-2 IgG binding N and RBD domain measured in the serum of NHPs using a multiplexed solid-phase chemiluminescence assay. Results are expressed in AU/mL. (B-E) Results are obtained after the initial exposure to SARS-CoV-2 at -24.9 weeks post-immunization (w.p.im) in convalescent (n=6, blue, dashed line) and α CD40.RBD-vaccinated convalescent (n=6, green, dotted line) animals and at 4 w.p.im in naive (n=6, black, solid line) animals. Thin lines represent individual values. Thick lines indicate medians within each group and shaded areas indicate 5th-95th confidence intervals. The red (-24.6 and 4.0 w.p.im) and blue (0 w.p.im) lines highlight viral exposure and vaccination respectively.

Figure 1 - figure supplement 2. Subgenomic viral dynamics after the second exposure to SARS-CoV-2.

Individual \log_{10} transformed subgenomic (gRNA) viral load dynamics in nasopharyngeal (top) and tracheal (bottom) swabs after the initial exposure to SARS-CoV-2 in naive macaques (n=6, black, right) and after the second exposure in convalescent (n=6, blue, middle) and α CD40.RBD-vaccinated convalescent (n=6, green, left) groups. Horizontal red dashed lines indicate the limit of quantification.

Figure 1 – figure supplement 3. Antibody measurements after the second exposure to SARS-CoV-2.

(A) Relative MFI of IgG binding to SARS-CoV-2 Spike protein, measured using a Luminex-based serology assay, in serum samples, after the second exposure to SARS-CoV-2. (B) Quantification of antibodies inhibiting that attachment of RBD domain or Spike protein to ACE2 receptor in NHP serum,

measured by the Mesoscale Discovery (MSD, Rockville, MD) pseudo-neutralization assay, after the second exposure to SARS-CoV-2. Results are expressed as ECL, in AU. **(C)** Quantification of SARS-CoV-2 IgG binding N or RBD domain measured in the serum of NHPs titrated by ELISA assay, after the second exposure to SARS-CoV-2. Results are expressed in Ig titer. **(D)** Quantification of SARS-CoV-2 IgG binding N or RBD domain measured in the serum of NHPs using a multiplexed solid-phase chemiluminescence assay, after the second exposure to SARS-CoV-2. Results are expressed in AU/mL. **(E)** Quantification of neutralizing antibodies against B.1.1.7, B.1.351 and D614G SARS-CoV-2 strains measured in the serum of NHPs using S-Fuse neutralization assay, after the second exposure to SARS-CoV-2 (measured only at the exposure and 20 days post-exposure (d.p.e)). Results are expressed as ED50 (Effective dose 50%). **(A-E)** Results are obtained after the initial exposure to SARS-CoV-2 in naive macaques (n=6, black, solid line) and after the second exposure in convalescent (n=6, blue, dashed line) and α CD40.RBD-vaccinated convalescent (n=6, green, dotted line) animals. Thin lines represent individual values. Thick lines indicate medians within each group and shaded areas indicate 5th-95th confidence intervals. Red dotted vertical lines highlight the viral exposure.

Figure 1 – figure supplement 4. Antigen-specific T-cell responses in NHPs after the second exposure to SARS-CoV-2.

(A-B) Frequency of IFN γ ⁺ (first line), IL-13⁺ (second line), IL-17⁺ (third line), IL-2⁺ (fourth line) or TNF α ⁺ (fifth line) antigen-specific CD4⁺ Tcells (CD154⁺) and CD8⁺ Tcells (CD137⁺) in the total CD4⁺ Tcell (A) or CD8⁺ Tcell (B) population in NHP serum. PBMCs were stimulated *ex-vivo* overnight with medium (left), SARS-CoV-2 RBD (middle) or N (right) overlapping peptide pools. T-cell responses being not measures at the challenge, measured obtained 14 days pre-exposure were added. **(C)** Antigen-specific T-cell responses in NHPs. T-cells were analyzed by ELISpot after *ex-vivo* stimulation with SARS-CoV-2 RBD or N overlapping peptide pools and plotted as spot-forming cells (SFC) per 1.0x10⁶ PBMCs. **(A-C)** Results are obtained after the initial exposure to SARS-CoV-2 in naive macaques (n=6, black, solid line) and after the second exposure in convalescent (n=6, blue, dashed line) and α CD40.RBD-vaccinated convalescent (n=6, green, dotted line) animals. Thin lines represent individual values. Thick lines indicate medians within each group and shaded areas indicate 5th-95th confidence intervals. Red dotted vertical lines highlight the viral exposure.

Figure 1 – figure supplement 5. Cytokines and chemokines in the plasma in NHPs after the second exposure to SARS-CoV-2.

Plasma concentration of 12 cytokines and chemokines in pg/mL. Results are obtained after the initial exposure to SARS-CoV-2 in naive macaques (n=6, black, solid line) and after the second exposure in

convalescent (n=6, blue, dashed line) and α CD40.RBD-vaccinated convalescent (n=6, green, dotted line) animals. Thin lines represent individual values. Thick lines indicate medians within each group and shaded areas indicate 5th-95th confidence intervals. Red dotted vertical lines highlight the viral exposure.

Figure 2 - figure supplement 1. Modelling of the viral dynamics using mechanistic model.

Examples simulated genomic viral load dynamics for different values of viral infectivity (β , left) or loss rate of infected cells (δ , right) showing the effect of either blocking de novo infection or promoting the destruction of infected cells on viral dynamics profile. Except for β or δ , all other parameters were fixed at a given value.

Figure 2 - figure supplement 2. Modelling of the dynamics of viral replication.

(A) Sagittal view of the 3D representation of the NHP respiratory system. (B) Coronal view of the 3D representation of the NHP respiratory system. (A-B) Lungs are colored in grey, Trachea and Nasal regions in blue and purple respectively. (C) Relationship between the weights (in kgs) measured in 4 NHPs and the estimation of the volume of their tracheal (blue circles) and nasal (orange triangles) regions (in cm^3). Measurements were obtained on NHPs similar to the 18 macaques of our study. Orange and blue dashed lines represent the step function used to describe this relationship with a breakpoint at 4.5 kg. (D) Volumes of the tracheal (blue circles) and nasal (orange triangles) regions estimated for the 18 macaques using the step function defined in the subfigure C and their weights. (E) Mean gRNA load dynamics in nasopharyngeal (left) and tracheal (right) swabs after the initial exposure to SARS-CoV-2 in naive macaques (n=6, black) and after the second exposure in convalescent (n=6, blue) and α CD40.RBD-vaccinated convalescent (n=6, green) macaques. Two additional macaques (IN + per Os, orange) were initially exposed to SARS-CoV-2 via intra-nasal (0.5mL of inoculum) and intra-gastric (4.5 mL) routes instead of intra-nasal (0.5 mL of inoculum) and intra-tracheal (4.5 mL) routes as defined in the study. Solid lines represent mean values and error bars indicate the 5th-95th confidence intervals.

Figure 4 – figure supplement 1. Immune markers selection and Basic reproduction number.

(A) *Systematic screening of effect of the markers (Step 2)*. For every single marker, a model, already adjusted on viral infectivity with antibodies inhibiting the attachment of RBD domain to ACE2 receptor, has been fitted to explore whether it explains the variation of the parameter of interest better or as well than the model of reference. Parameters of interest were β , the infection rate of ACE2+ target cells and δ , the loss rate of infected cells. Models were compared according to the Bayesian Information Criterion (BIC), the lower being the better. The red dashed line represents the reference model that includes the group effect (naive/ convalescent/vaccinated) on the parameter δ and with adjustment of pseudo-

neutralization on β . **(B) *Reproduction number at the time of exposure.*** Model predictions of the reproduction number at the time of exposure (R_0) in the tracheal (right) and nasopharyngeal (left) compartments for naive (black), convalescent (blue) and α CD40.RBD-vaccinated convalescent (green) animals. The reproduction number is representing the number of infected cells from one infected cell if target cells are unlimited. When this effective reproduction number is below 1, it means that the infection is going to be cured. The values of R_0 were estimated by the model with viral infectivity (β) and loss rate of infected cells (δ) adjusted on pseudo-neutralization and anti-RBD IgG binding antibodies titrated by ELISA assay respectively measured only at the time of challenge. Horizontal solid red lines highlight the threshold of the reproduction number equals to one.

Figure 4 - figure supplement 2. Flow chart of the algorithm for automatic selection of covariate.

At the initialization step of our study, the model without covariates is considered as initial the model, all immunological markers are seen as potential covariates (Marker) and $\{\beta, \delta\}$ is defined as the set of parameters on which covariates can be added. At each, all the marker-parameter relationships that have not already been added to the current model are added in an univariate manner to this model and ran. Among all the tested models, the one with the optimal value of selection criteria (e.g. lowest BICc) is selected (green dashed rectangle) and compared to the current model. If this one is better, it becomes the new current model and the algorithm moves to the step $k+1$. Otherwise, the algorithm stops.

Appendices

Appendix 1. Model building.

Appendix 2. BICc as selection criteria and multiple testing adjustment.

Supplementary Files

Supplementary file 1. Criteria defining neutralization as mechanistic correlate of protection of the effect of the vaccine on new cell infection.

Supplementary file 2. Model parameters estimated by the model adjusted for groups of intervention.

Supplementary file 3. Model parameters estimated by profile likelihood.

Supplementary file 4. Model parameters estimated by the model adjusted for RBD/ACE2 binding inhibition on beta and for groups on delta.

Figure 1 – source data 1. gRNA viral load longitudinally measured in the trachea and nasopharynx after the second exposure in the study 1.

Figure 1 – Source data 2. gRNA viral load longitudinally measured in the trachea and nasopharynx after the first exposure for convalescent NHPs in the study 1.

Figure 1 – Source data 3. Anti-spike IgG longitudinally measured post-immunization and quantified by Luminex in the study 1.

Figure 1 – Source data 4. Quantification of the Spike/ACE2 binding inhibition longitudinally measured post-immunization and quantified by MSD Assay (in 1/ECL) in the study 1.

Figure 1 – Source data 5. Anti-N and anti-RBD binding antibodies longitudinally measured post-immunization and quantified by MSD assay (in AU/mL) in the study 1.

Figure 1 – Source data 6. sgRNA viral load longitudinally measured in the trachea and nasopharynx after the second exposure in the study 1.

Figure 1 – Source data 7. Quantification of the neutralization function of antibodies against 3 variants (B117, B1351 and D614G) longitudinally measured post-exposition (in ED50) in the study 1.

Figure 1 – Source data 8. Antigen-specific T-cell response longitudinally measured post-exposure in % of CD4+ T cells measured by ICS in the study 1.

Figure 1 – Source data 9. Antigen-specific T-cell response longitudinally measured post-exposure in % of CD8+ T cells measured by ICS in the study 1.

Figure 1 – Source data 10. T-cell response expressing IFN- γ longitudinally measured post-exposure by ELISpot in the study 1.

Figure 1 – Source data 11. Cytokine concentrations measured post-exposure in the study 1.

Figure 2 – Source data 1. Volumes of the trachea and nasopharynx, and weights measured at the time of exposure in 4 NHPs in the study 1.

Figure 2 – Source data 2. Weights of the 18 NHPs in the study 1.

Figure 2 – Source data 3. gRNA viral load measured in the trachea and nasopharynx in the 2 additional NHPs receiving inoculum via intra-gastric and intra-nasal routes.

Figure 4 – Source data 1. Anti-N and anti-RBD binding antibodies longitudinally measured post-immunization and quantified by ELISA Assay in the study 1.

Figure 4 – Source data 2. Anti-RBD and anti-spike neutralizing antibodies longitudinally measured post-exposition and quantified by MSD Assay (in ECL) in the study 1.

Figure 5 – Source data 1. Anti-spike, anti-RBD and anti-N binding antibodies quantified by MSD assay (AU/mL), and quantification of the Spike/ACE2 binding inhibition by MSD assay (in 1/ECL), at the time of exposure in the study 2

1310 **Figure 5 – Source data 2.** gRNA and sgRNA viral loads longitudinally measured in the trachea and
1311 nasopharynx in the study 2.

Model building

In the model presented in the manuscript, we considered the two compartments of the upper respiratory tract (URT), trachea and nasopharynx, as two distinct compartments (i.e. without transfer of virus between them), as described by equation (1). In each of them, the viral dynamics are described by a target-cell limited model augmented with a compartment describing the dynamics of the inoculated virus (V_s). Moreover, in the statistical model describing the model parameters, the three parameters β , δ and P were assumed as jointly estimated between the two compartments, with shared random effects and covariates and considering that parameters β and δ are equal in both trachea and nasopharynx ($\beta^T = \beta^N$, $\delta^T = \delta^N$).

$$\left\{ \begin{array}{l} \frac{dT^N}{dt} = -\beta^N V_i^N T^N - \mu \beta^N V_s^N T^N \\ \frac{dI_1^N}{dt} = \beta^N V_i^N T^N + \mu \beta^N V_s^N T^N - k I_1^N \\ \frac{dI_2^N}{dt} = k I_1^N - \delta^N I_2^N \\ \frac{dV_i^N}{dt} = \mu P^N I_2^N - c V_i^N - \beta^N V_i^N T^N \\ \frac{dV_{ni}^N}{dt} = (1 - \mu) P^N I_2^N - c V_{ni}^N \\ \frac{dV_s^N}{dt} = -c_i V_s^N - \mu \beta^N V_s^N T^N \end{array} \right. \quad \left\{ \begin{array}{l} \frac{dT^T}{dt} = -\beta^T V_i^T T^T - \mu \beta^T V_s^T T^T \\ \frac{dI_1^T}{dt} = \beta^T V_i^T T^T + \mu \beta^T V_s^T T^T - k I_1^T \\ \frac{dI_2^T}{dt} = k I_1^T - \delta^T I_2^T \\ \frac{dV_i^T}{dt} = \mu P^T I_2^T - c V_i^T - \beta^T V_i^T T^T \\ \frac{dV_{ni}^T}{dt} = (1 - \mu) P^T I_2^T - c V_{ni}^T \\ \frac{dV_s^T}{dt} = -c_i V_s^T - \mu \beta^T V_s^T T^T \end{array} \right. \quad \# \quad (1)$$

Initially, random effects were added on the three parameters. However, taken into consideration identifiability issues that are usually encountered between the viral infectivity (β) and the viral production (P), we decided to remove the possibility of inter-individual variability on the parameter P . This choice was also driven by multiple model estimations showing less robust estimations when variability was allowed in both parameters β and P . In particular, the estimate of the viral production was impacted by a ratio between the parameter and its standard error (RSE) higher than 100%.

Comparison of the parameters between the tracheal and the nasopharyngeal compartments

To decide which of these three parameters were assumed to be equal between the two compartments, all possibilities were tested and compared, using the BICc as selection criteria. As shown in **Table 1**, we started with the model in which all parameters were equal between the two compartments and we progressively relaxed this hypothesis. During this step, no exchange of virions between the two

compartments of the URT was possible ($g=0$). Once all models estimated, we kept the one with the lowest value of BICc, meaning with the highest negative difference of BICc compared to the initial model. We identified the model with only the viral production varying between the two compartments as the best one to fit the data.

Table 1. Comparison of models evaluating the difference of viral infectivity (β), loss of infected cells (δ) and viral production (P) between the nasopharynx and the trachea.

Model tested	Statistical model	$\Delta BICc$
Initial model	$\beta^T = \beta^N$ $\delta^N = \delta^T$ $p^N = p^T$ Variability on β and δ	
Model with different β	$\beta^T \neq \beta^N$ $\delta^N = \delta^T$ $p^N = p^T$ Variability on β and δ	-17.31
Model with different δ	$\beta^T = \beta^N$ $\delta^N \neq \delta^T$ $p^N = p^T$ Variability on β and δ	-14.38
Model with different P	$\beta^T = \beta^N$ $\delta^N = \delta^T$ $p^N \neq p^T$ Variability on β and δ	-25.24
Model with different β and δ	$\beta^T \neq \beta^N$ $\delta^N \neq \delta^T$ $p^N = p^T$ Variability on β and δ	-13.00
Model with different β and P	$\beta^T \neq \beta^N$ $\delta^N = \delta^T$ $p^N \neq p^T$ Variability on β and δ	-19.19
Model with different δ and P	$\beta^T = \beta^N$ $\delta^N \neq \delta^T$ $p^N \neq p^T$ Variability on β and δ	-19.47
Model with different β , δ and P	$\beta^T \neq \beta^N$ $\delta^N \neq \delta^T$ $p^N \neq p^T$ Variability on β and δ	-13.39

Identification of group effects

Once the structure of the statistical model defined, we tried to identify on which parameters an effect of the group of treatment could be identified and by extension on which biological mechanisms. In this step, we were interested in four parameters: β , δ , P and c, the latter being the clearance of *de novo* produced

virions. In the study, three groups of treatments were considered as constant categorical covariates: Naïve, convalescent and convalescent vaccinated. We performed a forward selection approach using the BICc as selection criteria to find the best model, using the model without covariate as initial model. At each step the model decreasing the most the value of the BICc is selected and the procedure stops once the BICc does not decrease anymore. At each step of the procedure, the statistical significance of covariate added into the model was verified via a Wald test. As shown in **Table 2**, the selected model identified a group effect on the viral infectivity and the loss rate of infected cells.

Table 2. Comparison of models evaluating the adjustment of the viral infectivity (β), the loss rate of infected cells (δ), the viral production (P) and the viral clearance (c) for the groups of treatment. The group of naïve animals is assumed as the group of reference.

Step	Model tested	Statistical model	$\Delta BICc$
1	Initial Model: Model without group effects	$\beta = 10^{(\beta_0)}$ $\delta = \delta_0$ $P = P_0$ $c = c_0$	
	Model with group effect on β	$\beta = 10^{(\beta_0 + \phi_{conv}^\beta + \phi_{CD40}^\beta)}$ $\delta = \delta_0$ $P = P_0$ $c = c_0$	-21.5
	Model with group effect on δ	$\beta = 10^{\beta_0}$ $\delta = \delta_0 \exp(\phi_{conv}^\delta + \phi_{CD40}^\delta)$ $P = P_0$ $c = c_0$	-16.62
	Model with group effect on P	$\beta = 10^{\beta_0}$ $\delta = \delta_0$ $P = P_0 \exp(\phi_{conv}^P + \phi_{CD40}^P)$ $c = c_0$	+9.68
	Model with group effect on c	$\beta = 10^{\beta_0}$ $\delta = \delta_0$ $P = P_0$ $c = c_0 \exp(\phi_{conv}^c + \phi_{CD40}^c)$	+9.20
2	Initial Model: Model with group effect on β	$\beta = 10^{(\beta_0 + \phi_{conv}^\beta + \phi_{CD40}^\beta)}$ $\delta = \delta_0$ $P = P_0$ $c = c_0$	
	Model with group effect on β and δ	$\beta = 10^{(\beta_0 + \phi_{conv}^\beta + \phi_{CD40}^\beta)}$ $\delta = \delta_0 \exp(\phi_{conv}^\delta + \phi_{CD40}^\delta)$ $P = P_0$ $c = c_0$	-2.48
	Model with group effect on β and P	$\beta = 10^{(\beta_0 + \phi_{conv}^\beta + \phi_{CD40}^\beta)}$ $\delta = \delta_0$ $P = P_0 \exp(\phi_{conv}^P + \phi_{CD40}^P)$ $c = c_0$	+12.25
	Model with group effect on β and c	$\beta = 10^{(\beta_0 + \phi_{conv}^\beta + \phi_{CD40}^\beta)}$ $\delta = \delta_0$ $P = P_0$ $c = c_0 \exp(\phi_{conv}^c + \phi_{CD40}^c)$	+11.97

3	Initial Model: Model with group effect on β and δ	$\beta = 10^{\beta_0 + \phi_{conv}^{\beta} + \phi_{CD40}^{\beta}}$ $\delta = \delta_0 \exp(\phi_{conv}^{\delta} + \phi_{CD40}^{\delta})$ $P = P_0$ $c = c_0$	
	Model with group effect on β , δ and P	$\beta = 10^{\beta_0 + \phi_{conv}^{\beta} + \phi_{CD40}^{\beta}}$ $\delta = \delta_0 \exp(\phi_{conv}^{\delta} + \phi_{CD40}^{\delta})$ $P = P_0 \exp(\phi_{conv}^P + \phi_{CD40}^P)$ $c = c_0$	+10.88
	Model with group effect on β , δ and c	$\beta = 10^{\beta_0 + \phi_{conv}^{\beta} + \phi_{CD40}^{\beta}}$ $\delta = \delta_0 \exp(\phi_{conv}^{\delta} + \phi_{CD40}^{\delta})$ $P = P_0$ $c = c_0 \exp(\phi_{conv}^c + \phi_{CD40}^c)$	+11.61

46

47 Based on all these results, the optimal statistical model with adjustment for groups of treatment was defined
48 as follows:

$$\begin{cases} \log_{10}(\beta_i) = \beta_0 + \phi_{conv}^{\beta} \times \mathbb{I}_{i \in conv} + \phi_{CD40}^{\beta} \times \mathbb{I}_{i \in CD40} + u_i^{\beta} \\ \log(\delta_i) = \log(\delta_0) + \phi_{conv}^{\delta} \times \mathbb{I}_{i \in conv} + \phi_{CD40}^{\delta} \times \mathbb{I}_{i \in CD40} + u_i^{\delta} \\ \log(P_i^N) = \log(P_0) \\ P_i^T = P_i^N \times \exp(f_P^T) \end{cases}$$

49

50 Exchange of viruses between the nasopharyngeal and tracheal compartments

51 Afterwards, we tested the possibility of an exchange of free plasma virus from between the two
52 compartments of the URT. We made the hypothesis of a constant first order exchange and we tested the
53 addition a transfer of virions from nasopharyngeal to tracheal compartments and vice versa, with a migration
54 rate g_{NT} and g_{TN} respectively. To this end, equations of infectious (V_i) and non-infectious (V_{ni}) viruses in
55 Equation (1) between the two compartments were linked as follows:

$$\begin{aligned} \frac{dV_i^T}{dt} &\mapsto \frac{dV_i^T}{dt} - g_{TN}V_i^T + g_{NT}V_i^N & \frac{dV_{ni}^T}{dt} &\mapsto \frac{dV_{ni}^T}{dt} - g_{TN}V_{ni}^T + g_{NT}V_{ni}^N \\ \frac{dV_i^N}{dt} &\mapsto \frac{dV_i^N}{dt} + g_{TN}V_i^T - g_{NT}V_i^N & \frac{dV_{ni}^N}{dt} &\mapsto \frac{dV_{ni}^N}{dt} + g_{TN}V_{ni}^T - g_{NT}V_{ni}^N \end{aligned} \quad (2)$$

56 with the arrow symbolizing the modification of the equations defined in (1) and g_{NT} and g_{TN} being two
57 positive rates. As a first step, we tried to estimate either bidirectional or one of the two unidirectional
58 transfers using the data from the 18 NHPs of the first study described in the main paper. However, data were
59 too spare to bring enough information to get estimations. Consequently, as a second step, additional data
60 were used: two naïve macaques were exposed to the same dose (1×10^6 pfu) of SARS-CoV-2 than the 18
61 NHPs of the main study. However, instead of being inoculated via intra-tracheal (4.5 mL) and intra-nasal
62 (0.5 mL) routes, these latter received inoculum via intra-gastric (4.5 mL) and intra-nasal (0.5 mL) routes.

Similar to the main study, the viral gRNA dynamics in both tracheal and nasopharyngeal compartments were repeatedly measured during the 20 days following the challenge (**Figure S9E**).

These two additional macaques having not received intra-tracheal inoculum, viral dynamics measured in this same compartment was expected to come from (at least partially) an exchange with the nasopharynx and thus bring information about it. However, having only two macaques without virions inoculated via intra-tracheal route, no enough information were available to totally estimate the model with exchanges. Consequently, these two additional NHPs having similar characteristics than the 18 NHPs involved in the main study, we made the assumption that the viral dynamics in nasopharynx after inoculation and the viral dynamics in the trachea, once the transfer initiated, should be described by the same model (without inoculum in trachea) and those by the same parameters. We expected that the difference of dynamics in trachea between these two set of macaques could allow an estimation of the parameters g_{TN} and/or g_{NT} . For that reason, we estimated the model in equation (1) using data from the 18 NHPs of the main study. Then using the data from the two additional NHPs, and assuming all parameters of the model resulting from equations (2) as fixed (see **Table S2**), except g_{TN} and g_{NT} , we tried to quantify the transfers of virions.

The estimation of multiple models on those two animals tended to conclude that only a unidirectional transfer of viruses from the nasopharyngeal to the tracheal compartment should be explored, with an estimation of g_{NT} ranging from 0.9 to 2.5 day⁻¹. Once these values quantified, we tried to update/re-estimate the model, initially estimated on the 18 NHPs, using only a unidirectional transfer from nasopharynx to trachea and fixing the value of the migration rate at the different values aforementioned. However, all tested values of g_{NT} led irremediably to a degradation of the model with an increase of at least 2 points of BICc.

An estimation of the parameter g_{NT} by profile likelihood (results not shown) led to a strictly increasing profile of the likelihood (the lower the better) and was thus no more conclusive. Consequently, no exchange of virions were assumed in the final model and the parameters g_{NT} and g_{TN} were fixed at 0 day⁻¹.

BICc as selection criteria and multiple testing adjustment

In the case of classic covariate selection approaches using p-values as selection criteria, particular attention must be paid to take into account the dependence of the results on the number tests performed.

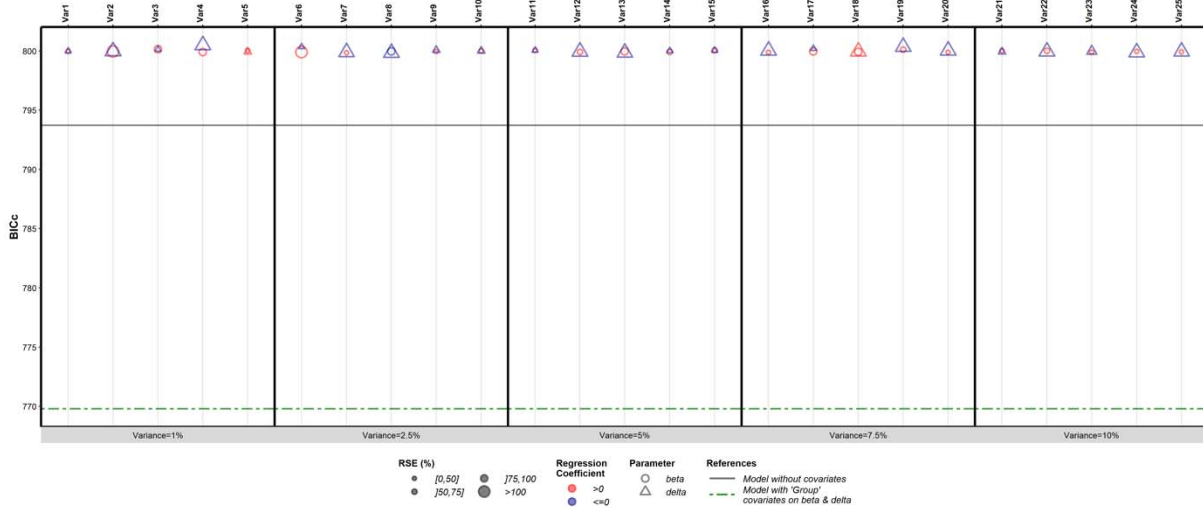
Over the years, multiple corrections have been proposed to adjust results for test multiplicity (e.g. Bonferroni correction, Benjamini & Hochberg correction among others).

Although we verified the significance of the covariate selected in our model, our covariate selection approach relies on the corrected Bayesian information criteria (BICc). To ensure the robustness of the BICc as selection criterion despite the multiplicity of the tests, we performed an additional simulation work.

We simulated $M=25$ longitudinal variables for 18 individuals and with similar time points than those found on our data, meaning at days 0, 4, 9 and 20 post-infection. Variables were simulated as white noise random variables such that for the i th subject at the j th time point, the m th variable was defined as $X_{ij}^m \sim \mathcal{N}(0, \sigma^2)$, with $m = 1, \dots, M$. In our simulations, we tested 5 values for the variance σ^2 ranging from 1 to 10% (5 variables simulated for each value of σ).

Assuming these variables as our time-varying covariates, we applied the forward selection approach used in our method by testing each of them in a univariate manner of both β and δ .

As shown in **Appendix2 - figure 1**, the 50 models built to evaluate the adjustment of either β or δ for the simulated variables provide similar results in term of BICc, and thus whatever the value of the standard deviation σ used. Consequently, these results appear as quite robust to the multiplicity of the test. Moreover, as expected, adjustments for white-noise random variables depict the degradation of the model in comparison to the model without covariates.



Appendix2 - figure 1. Results of the forward selection approach applied on the 25 simulated white-noise random variables. The discrete x-axis represents the different variables and the y-axis represents the values of the BICc. Circles and triangles correspond to the results obtained with the parameters β or δ adjusted for the variables. The horizontal solid black line represents the value of the BICc obtained with the model without covariates while the horizontal dashed green line highlights the value of the criterion obtained with both β and δ adjusted for the groups of treatment.

Evaluation of the robustness of the estimation

To evaluate the robustness of the parameter estimates obtained on our models, despite the small number of independent observations, we performed a bootstrap procedure with replacement (79), for $B=50$ iterations. The bootstrap parameter estimate was calculated as the median of the parameter estimates from the B bootstrap samples while the standard error of each parameter was calculated according to the definition of Thai et al. (2013) (79), which means with the SE of the l -th component of the vector of parameters given by:

$$\widehat{SE}_B^{(l)} = \sqrt{\frac{1}{B-1} \sum_{b=1}^B \left(\hat{\theta}_b^{*(l)} - \hat{\theta}_B^{(l)} \right)^2}$$

with $\hat{\theta}_b^{*(l)}$ being its estimate obtained at the b -th iteration of the bootstrap and $\hat{\theta}_B^{(l)}$ the bootstrap parameter estimate. For each bootstrap sample, we paid attention to keep the 1:1:1 ratio between the 3 groups of treatment, with 6 animals selected within each group. Results are reported in **Appendix 2 - Table 1** and **Appendix 2 - Table 2**.

42 **Appendix 2 - Table 1.** Model parameters for viral dynamics in both the nasopharynx and the trachea estimated by the model adjusted for groups of
43 intervention. For the bootstrap procedure, 50 iterations were performed.

Param.	Meaning	Value [95% CI]	Unit
β	Viral infectivity in the naive group ($\times 10^{-6}$)	0.91 [0.12 ; 7.03]	(copies/ml) ⁻¹ day ⁻¹
	Fold change in the convalescent group	0.15 [0.04 ; 0.58]	
	Fold change in the Conv-CD40 group	0.006 [0.001 ; 0.04]	
δ	Loss rate of infected cells in the naive group	1.09 [0.74 ; 1.60]	day ⁻¹
	Fold change in the convalescent group	1.70 [1.08 ; 2.66]	
	Fold change in the Conv-CD40 group	2.00 [0.94 ; 4.27]	
P^N	Viral production rate in the naso. ($\times 10^3$)	10.1 [1.16 ; 87.7]	virions.(cell.day) ⁻¹
P^T	Viral production rate in the trachea ($\times 10^3$)	0.86 [0.08 ; 9.19]	virions.(cell.day) ⁻¹
α_{vls_g}	Infected cells and sgRNA viral load ratio	1.42 [0.99 ; 2.02]	Virions.cell ⁻¹
k	Eclipse rate	3	day ⁻¹
c	Clearance of <i>de novo</i> produced viruses	3	day ⁻¹
c_I	Clearance of inoculum	20	day ⁻¹
μ	Percentage of infectious viruses	10^{-3}	
$T_0^{X,nbc}$	Initial number of target cells	1.25x10 ⁵ (Naso.)	cells
		2.25x10 ⁴ (Trachea)	
$Inoc_0$	Number of virions inoculated	2.19x10 ¹⁰	virions
ω_β	SD of random effect on log ₁₀ β	0.319 [0.111 ; 0.527]	
ω_δ	SD of random effect on δ	0.122 [-0.039 ; 0.283]	
σ_{VLn}	SD of error model gRNA in naso.	1.24 [0.96 ; 1.51]	
σ_{VLt}	SD of error model gRNA in trachea	1.09 [0.92 ; 1.26]	
σ_{sgVLn}	SD of error model sgRNA in naso	1.35 [1.08 ; 1.61]	
σ_{sgVLt}	SD of error model sgRNA in trachea	1.53 [1.15 ; 1.92]	

46 **Appendix 2 - Table 2.** Model parameters for viral dynamics in both the nasopharynx and the trachea estimated by the model with the viral infectivity
47 adjusted for ACE2-RBD binding inhibition and the loss rate of infected cells adjusted for the group of treatment. For the bootstrap procedure, 50
48 iterations were performed.

Param.	Meaning	Value [95% CI]	Unit
β	Infection rate with ECLRBD=0 AU ($\times 10^{-8}$)	0.82 [0.13 ; 5.13]	(copies/ml) ⁻¹ day ⁻¹
	Fold Δ ECLRBD = 10^3 AU	1.017 [1.012 ; 1.022]	
δ	Loss rate of infected cells	1.02 [0.80 ; 1.30]	day ⁻¹
	Fold change in the convalescent group	1.74 [1.24 ; 2.46]	
	Fold change in the Conv-CD40 group	2.17 [0.82 ; 5.74]	
P^N	Viral production rate in the naso. ($\times 10^3$)	8.92 [0.42 ; 191]	virions.(cell.day) ⁻¹
P^T	Viral production rate in the trachea ($\times 10^3$)	0.62 [0.02 ; 19.7]	virions.(cell.day) ⁻¹
a_{vls}	Infected cells and sgRNA viral load ratio	1.32 [0.91 ; 1.90]	Virions.cell ⁻¹
k	Eclipse rate	3	day ⁻¹
c	Clearance of <i>de novo</i> produced viruses	3	day ⁻¹
c_I	Clearance of inoculum	20	day ⁻¹
μ	Percentage of infectious viruses	10^{-3}	
$T_0^{X,nbc}$	Initial number of target cells	1.25x10 ⁵ (Naso.)	cells
		2.25x10 ⁴ (Trachea)	
$Inoc_0$	Number of virions inoculated	2.19x10 ¹⁰	virions
ω_β	SD of random effect on log ₁₀ β	0.205 [0.011 ; 0.399]	
ω_δ	SD of random effect on δ	0.079 [-0.092 ; 0.250]	
σ_{VLn}	SD of error model gRNA in naso.	1.13 [0.90 ; 1.36]	
σ_{VLt}	SD of error model gRNA in trachea	1.27 [1.07 ; 1.48]	
σ_{sgVLn}	SD of error model sgRNA in naso	1.62 [1.30 ; 1.94]	
σ_{sgVLt}	SD of error model sgRNA in trachea	1.36 [1.15 ; 1.56]	

Figure 1

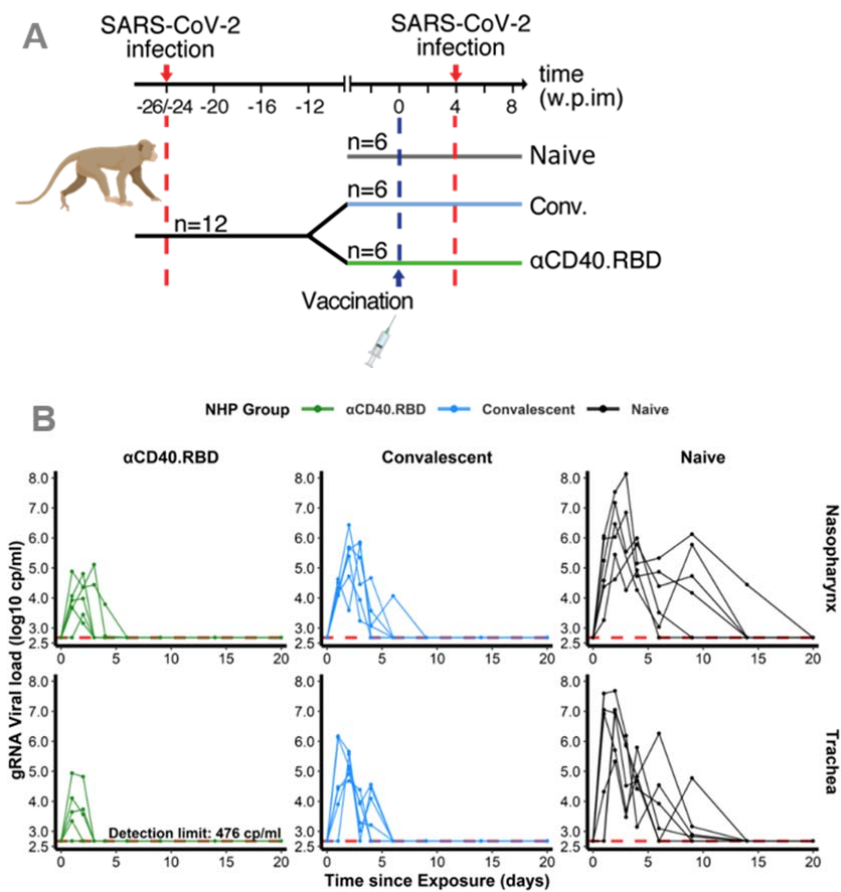


Figure 2

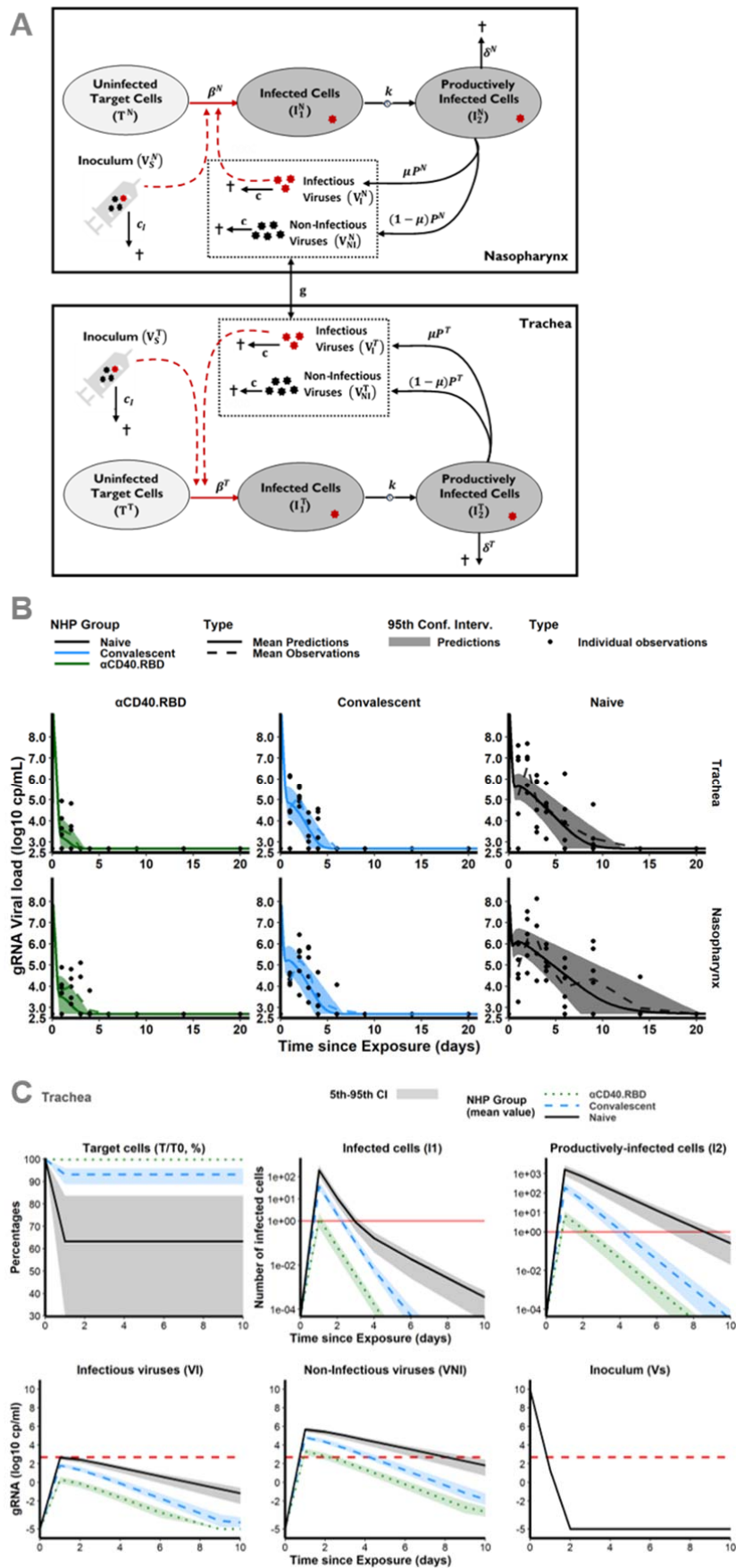


Figure 3

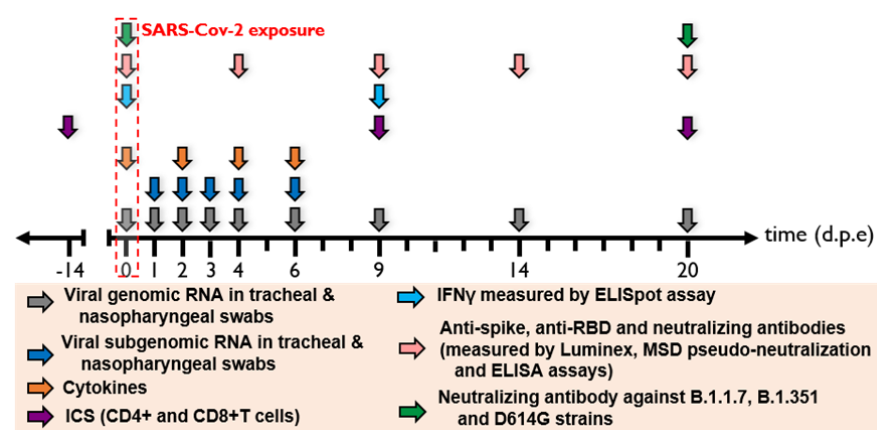


Figure 4

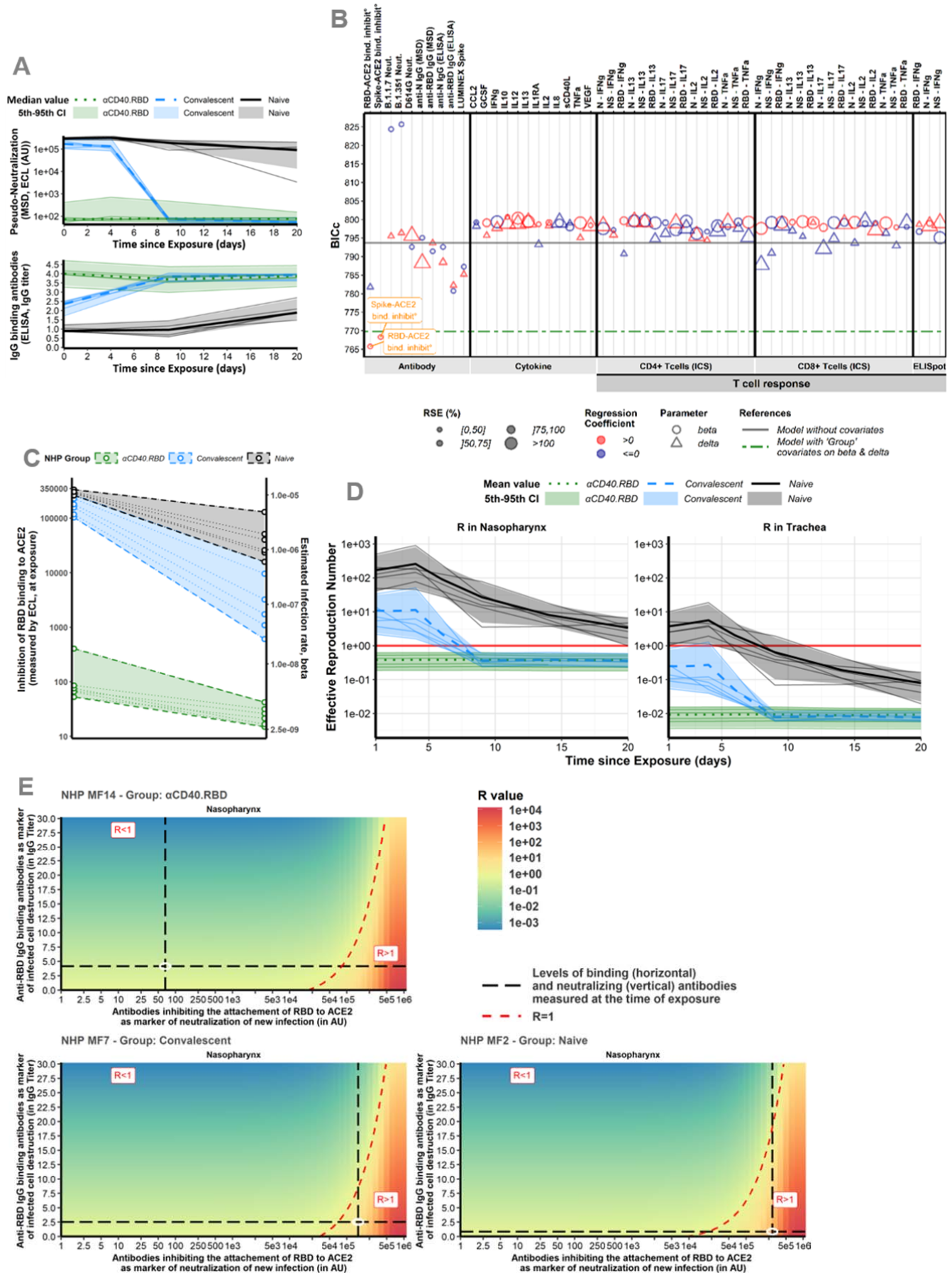
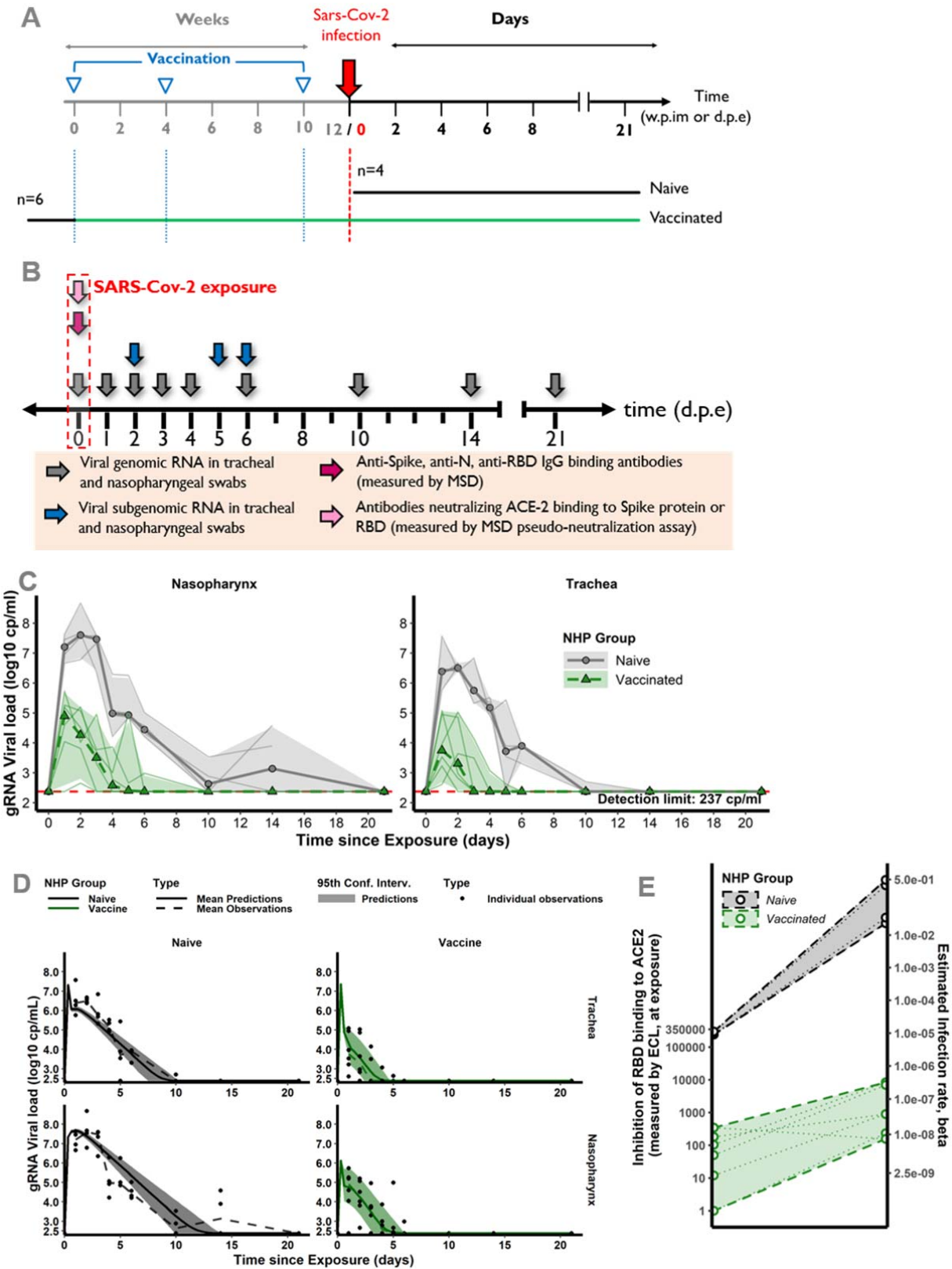


Figure 5



Appendix 2 – Figure 1.

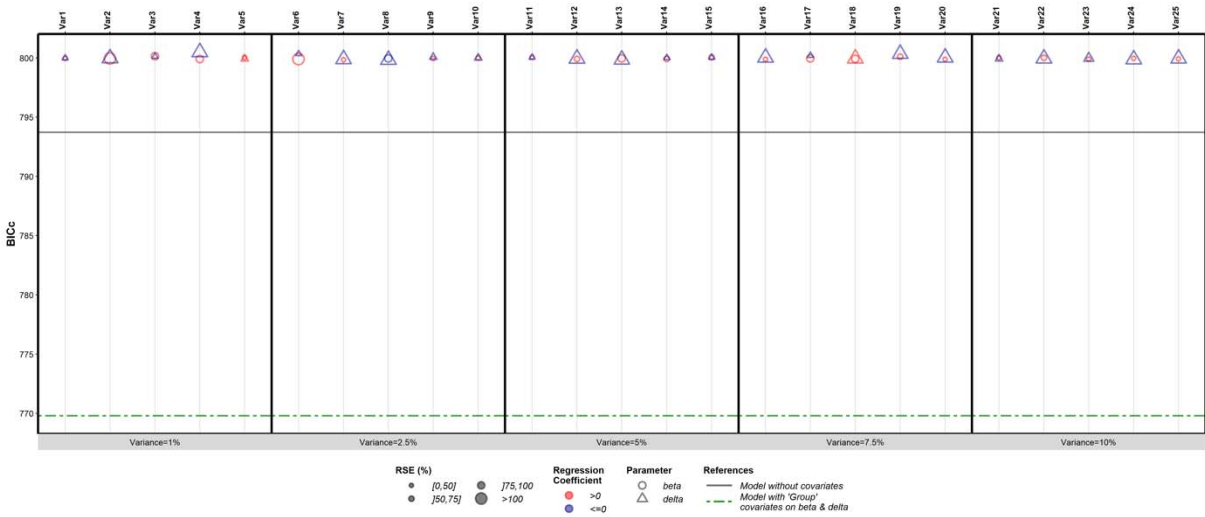


Figure 1 – figure supplement 1

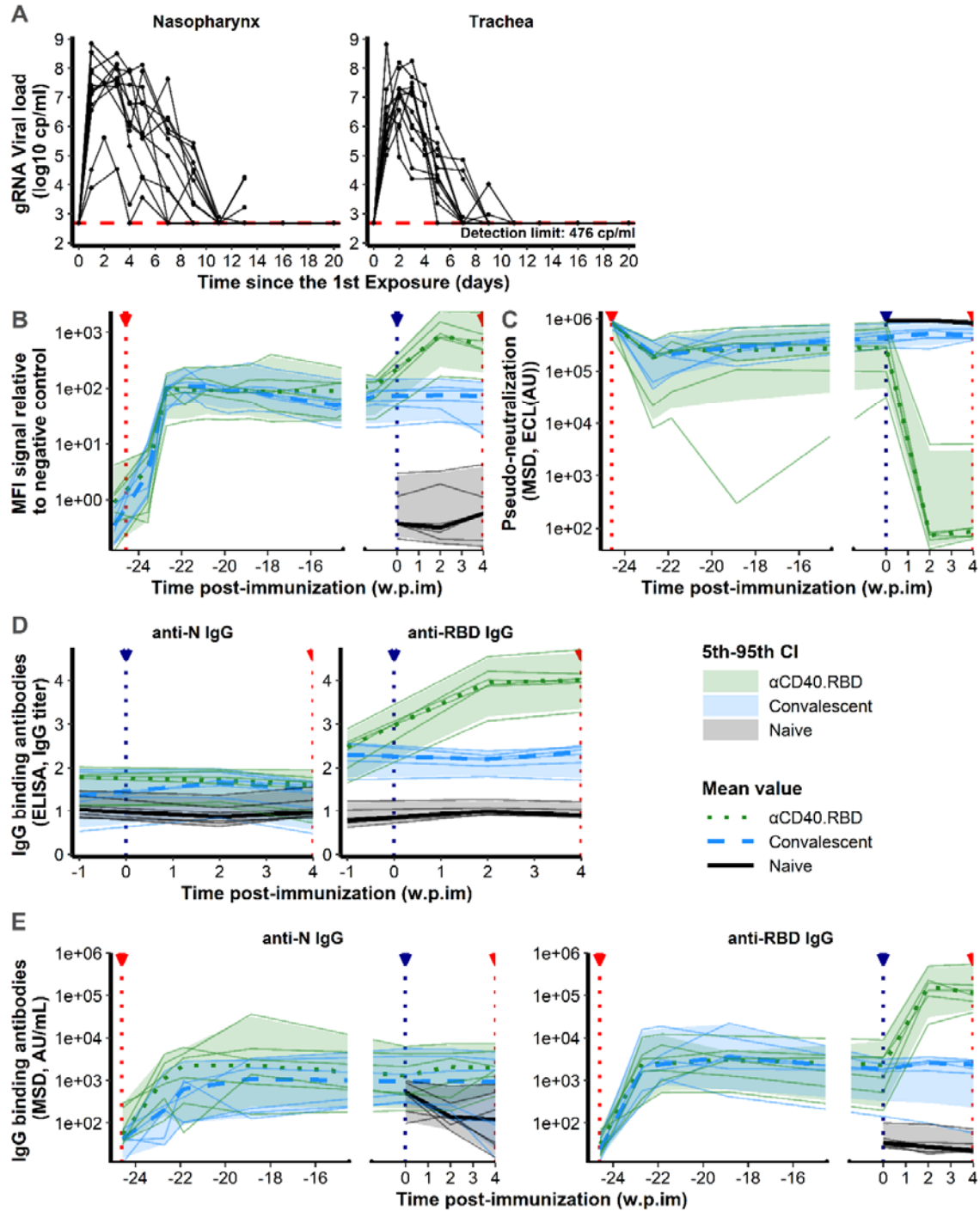


Figure 1 – figure supplement 2

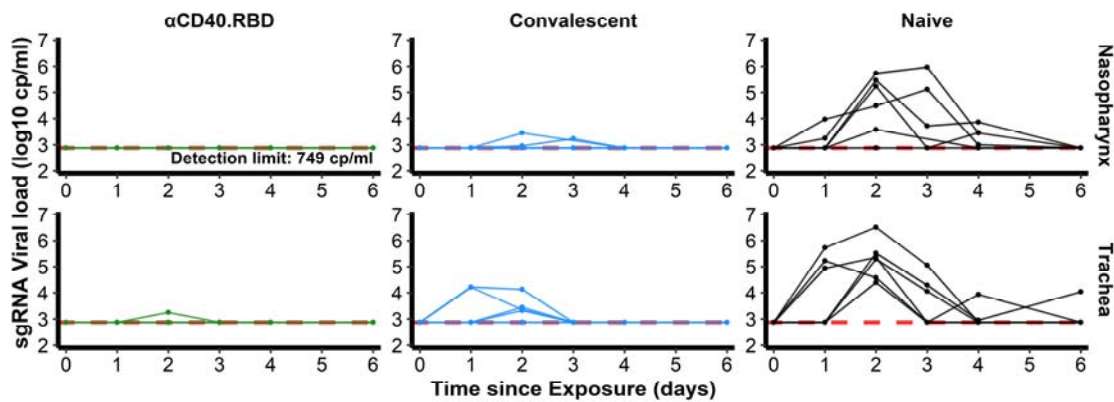


Figure 1 – figure supplement 3

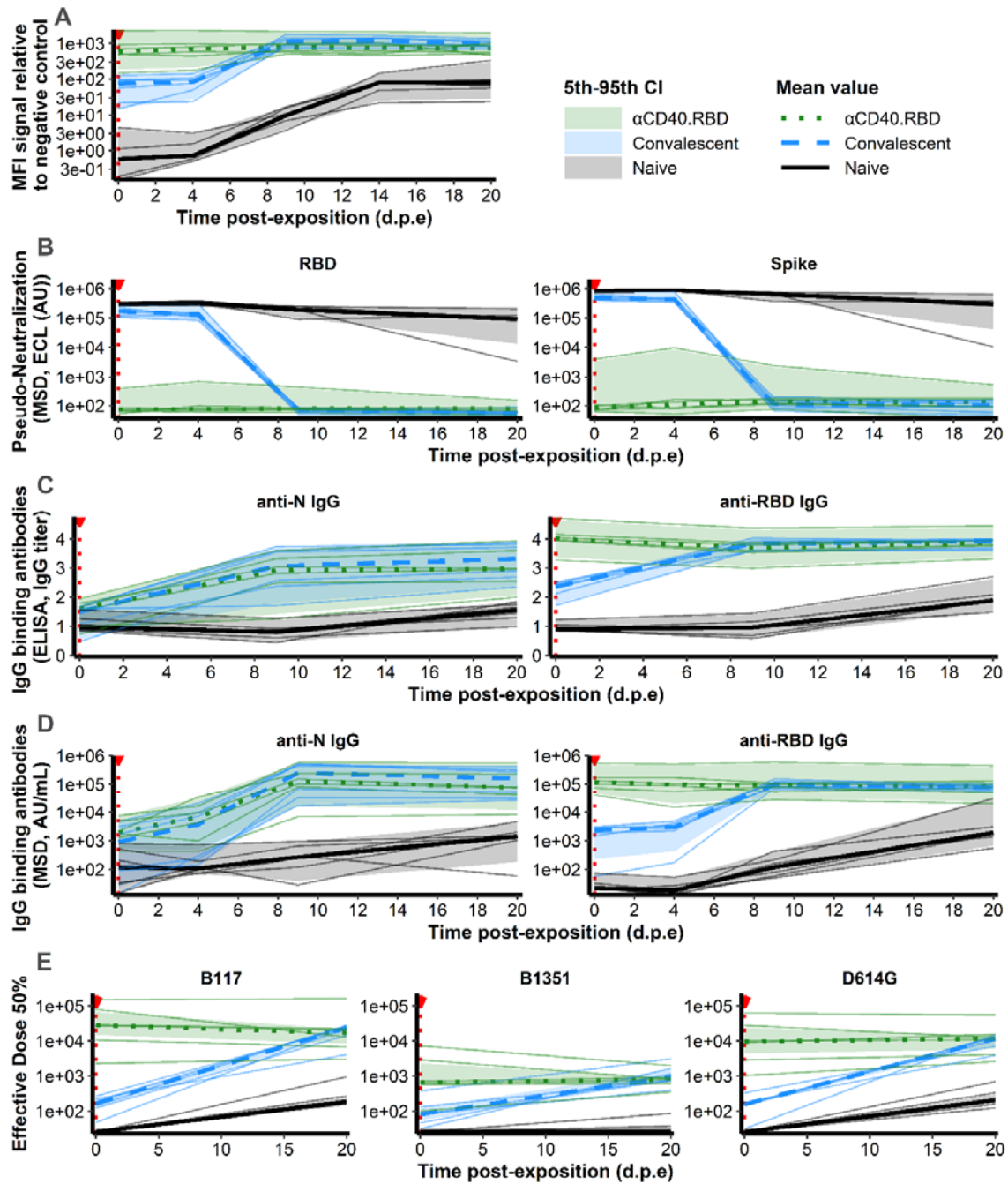


Figure 1 – figure supplement 4

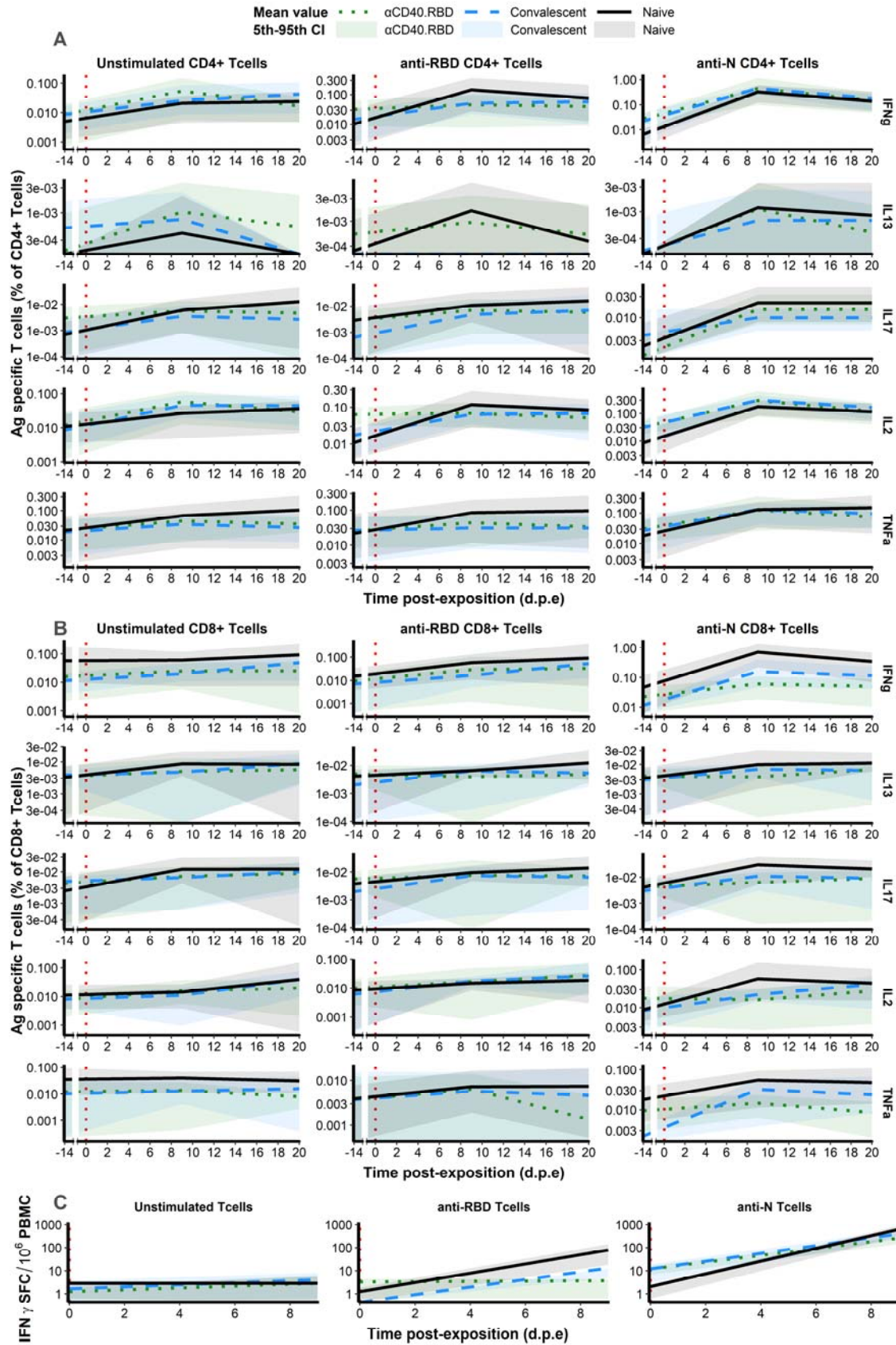


Figure 1 – figure supplement 5

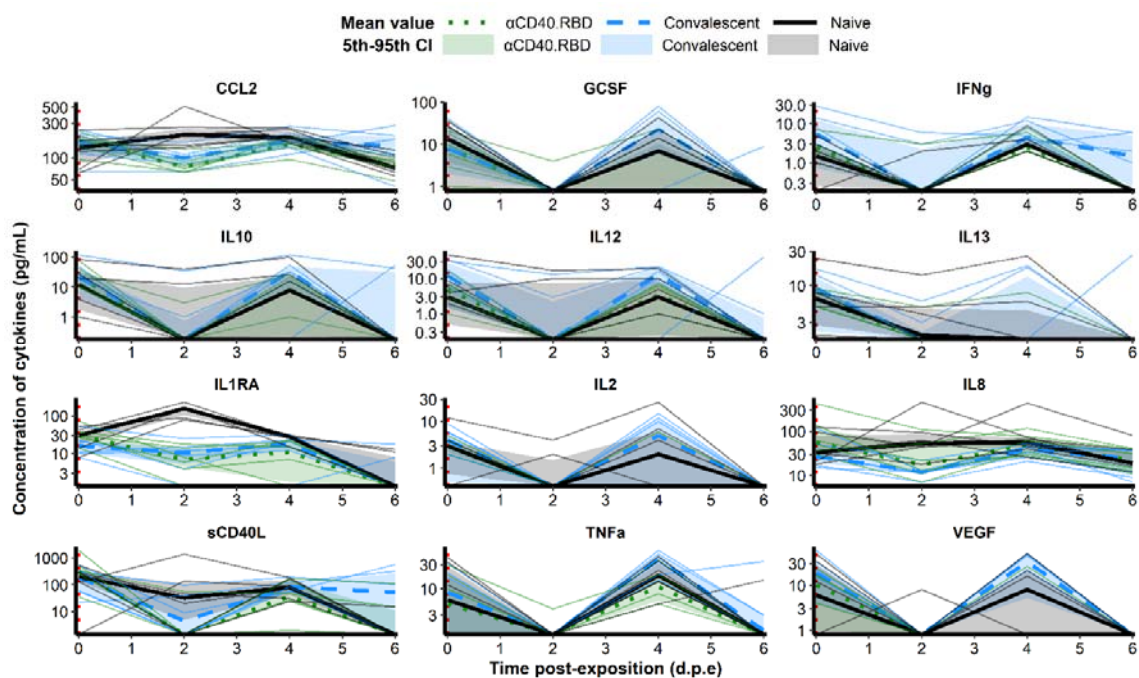


Figure 2 – figure supplement 1

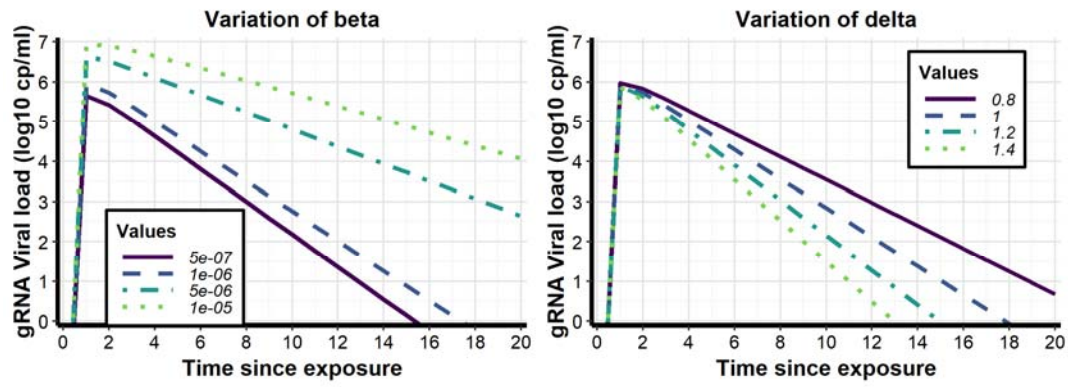


Figure 2 – figure supplement 2

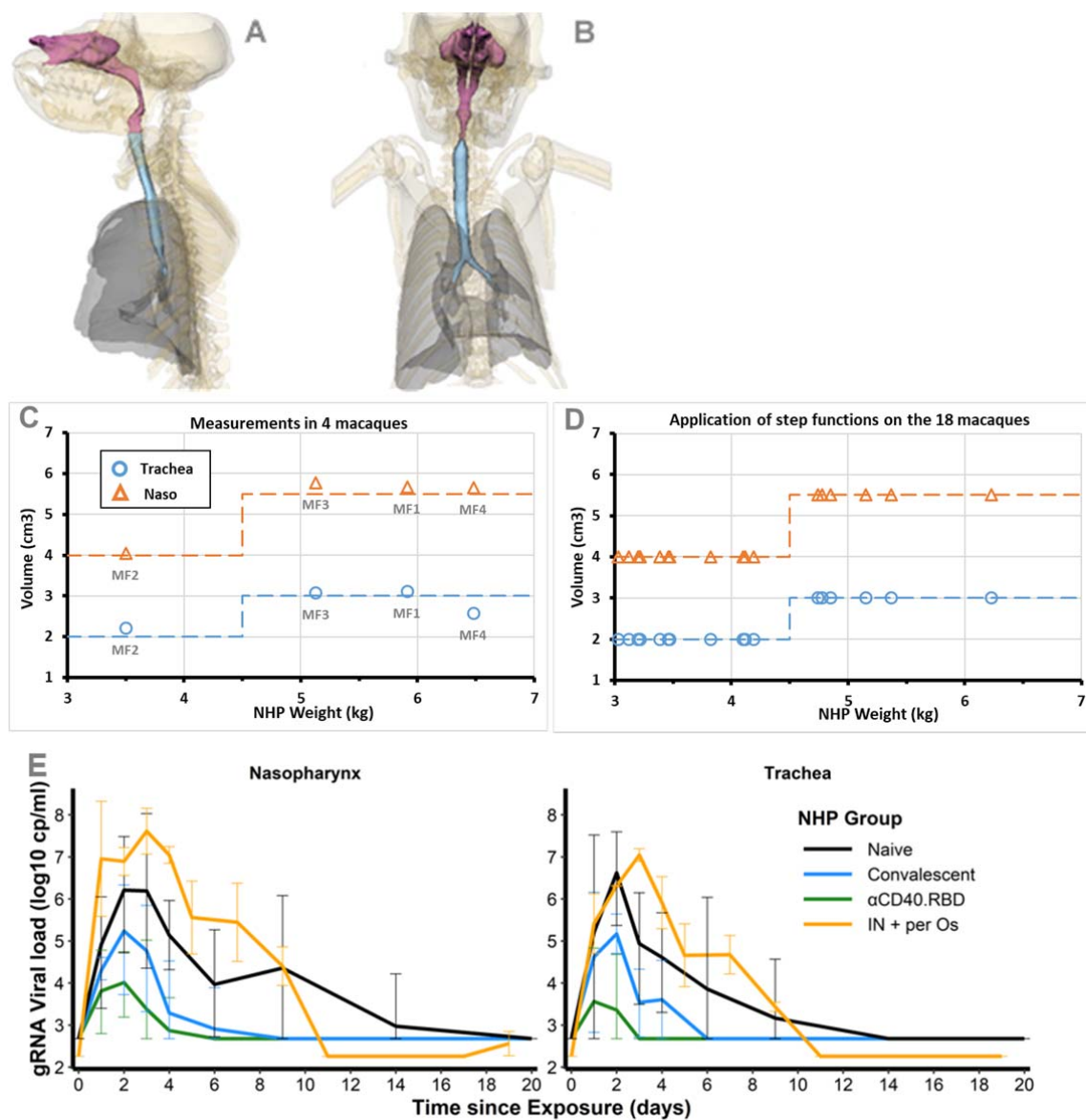


Figure 4 – figure supplement 1

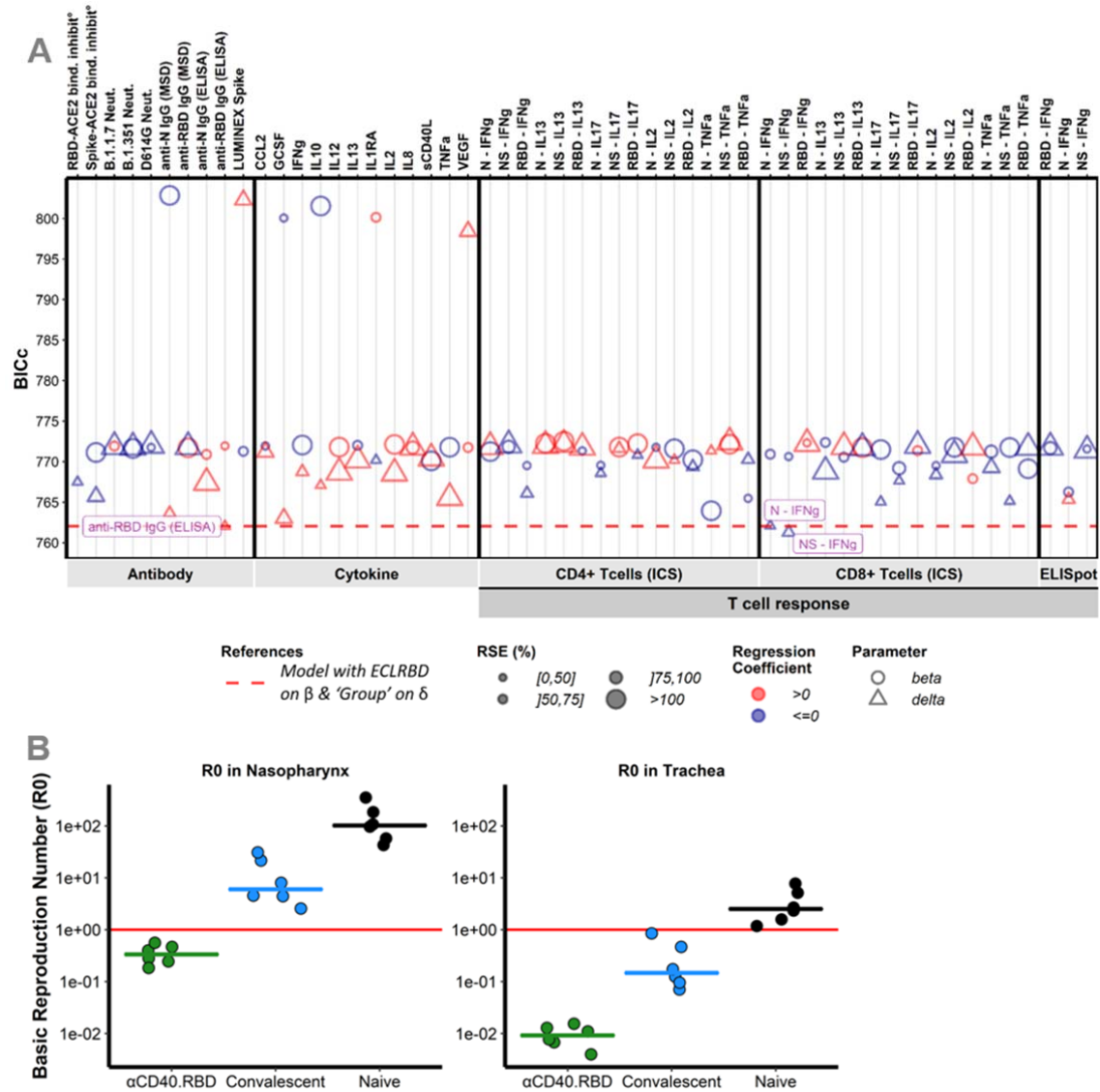


Figure 4 – figure supplement 2

